Journal of Volcanology and Geothermal Research 444 (2023) 107935

Contents lists available at ScienceDirect

Journal of Volcanology and Geothermal Research

journal homepage: www.journals.elsevier.com/journal-of-volcanology-and-geothermal-research

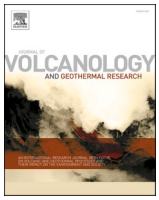

Benchmarking a new 2.5D shallow water model for lava flows

Elisa Biagioli [a,*], Mattia de' Michieli Vitturi [b], Fabio Di Benedetto [c,1], Margherita Polacci [a]

[a] Department of Earth and Environmental Sciences, University of Manchester, Williamson Building, Oxford Road, Manchester M13 9PL, UK
[b] Istituto Nazionale di Geofisica e Vulcanologia INGV, Sezione di Pisa, Via Cesare Battisti, 53, Pisa 56125, Italy
[c] Department of Mathematics, University of Genoa, Via Dodecaneso 35, Genoa 16146, Italy

ARTICLE INFO

Keywords:
Lava flows modelling
Heat transfer modelling
Temperature-dependent viscosity
Viscoplastic viscosity model
Depth-averaged model
Velocity and temperature profiles

ABSTRACT

Lava flows associated with effusive volcanic eruptions require accurate modelling in order to forecast potential paths of destruction.

This study presents a new depth-averaged model that overcomes the classical shallow water hypothesis by incorporating several enhancements, allowing for a more precise representation of the flow dynamics and behaviour: (*i*) a parabolic profile which captures the vertical variations in velocity within the flow; (*ii*) a non-constant vertical profile for temperature, enabling a more realistic representation of thermal gradients within the flowing lava; (*iii*) a viscoplastic temperature-dependent viscosity model to account for the non-Newtonian behaviour of lava; (*iv*) a transport equation for temperature accounting for the thermal heat exchanges with the environment and the soil. The first two modifications allow us to describe, under reasonable assumptions, the vertical structure of the flow, and for this reason, we put our model in the class of 2.5D models.

To assess the performance of our modified model, comprehensive benchmark tests are conducted using both laboratory experiments and real-world lava flow data related to the 2014–2015 Pico do Fogo, Cape Verde, effusive eruption. The benchmarking analysis demonstrates that this model accurately reproduces, with short execution times, essential flow features such as flow front advancement and cooling processes.

1. Introduction

Volcanic eruptions are among Earth's most powerful natural phenomena and threaten people living near them. Eruptions may display explosive activity with the ejection of gas and pyroclastic material into the atmosphere, or effusive activity with the propagation of a lava flow from the vent, or both. Lava flows see behaviours that depend on different effusion rates, temperatures, and lava's chemical-physical composition, which may change from eruption to eruption and even during different phases of a single eruption, strongly affecting lava viscosity. For example, during the eruption of the 2014–2015 eruption at Holuhraun, Iceland, the first phase had a discharge rate in the range of 100–350 $m^3 s^{-1}$ with an averaged lava flow velocity of 44.27 $m h^{-1}$, and the second phase was characterized by a discharge rate in the range of 50–100 $m^3 s^{-1}$ and average propagation velocity of 11.35 $m h^{-1}$ (Pedersen et al., 2017). In most cases, volcano observatories and civil protection have time to respond promptly once the effusive event is underway by evaluating the current and potential event scenarios and preparing evacuation and safety plans if needed. Before an eruptive event, short-term hazard maps forecasting future scenarios can be generated. A priori study is one of the few preventive actions possible in the case of a very rapid lava flow, which is a rarer event to consider anyway. As an example, we remind the 1977 eruption of Nyiragongo, which recorded lava flow speeds of up to 60 km per hour (Nakamura and Aoki, 1980). Therefore, reliable forecasting of lava flow paths is a fundamental tool for improving volcanic hazard and risk mitigation, and requires a quantitative description of the effusive phenomenon.

In the 1970s, the traditionally qualitative and observation-oriented field of Volcanology started transforming into a quantitative science. Modern volcanologists started to investigate volcanic eruptions behind visible phenomena, turning to physical and mathematical models to better understand their dynamics. The first generations of numerical models for volcanic processes were analytical and 1D models, in general steady-state. More recently, advancement in the physical processes description with new mathematical models and the increased computational resources allowed the development of more complex

* Corresponding author.
E-mail addresses: elisa.biagioli@manchester.ac.uk (E. Biagioli), mattia.demichielivitturi@ingv.it (M. de' Michieli Vitturi), dibenede@dima.unige.it (F. Di Benedetto), margherita.polacci@manchester.ac.uk (M. Polacci).
[1] Member of Research Group GNCS-INDAM.

https://doi.org/10.1016/j.jvolgeores.2023.107935
Received 23 June 2023; Received in revised form 9 October 2023; Accepted 12 October 2023
Available online 21 October 2023

Computational Fluid Dynamics (CFD) models leading to transient and 2D/3D models. However, as far as lava flows are concerned, only a small number of transient and multidimensional numerical models have been developed so far because of the complexity, variability, and uncertainties in the physical phenomenon.

Lava flow models should account for both fluid dynamics and thermal effects through the solution of the mass, momentum and energy conservation equations. In addition to the conservation laws, a lava flow emplacement model should consider other factors (Cordonnier et al., 2015).

(i) Firstly, an accurate and updated topography description and the precise vent position are among the major factors in forecasting the correct lava flow emplacement (Bilotta et al., 2019; Flynn et al., 2023). Slight differences in the vent location or the topography may lead to significant variations in the resulting simulation.
(ii) Secondly, eruptive input conditions, such as effusion rate, effusive temperature, and vent geometry, affect the emplacement (Harris and Rowland, 2009; Lister, 1992).
(iii) Additionally, lava's physical properties, such as density and rheology, have a major influence on the dynamics (Pinkerton and Wilson, 1994).
(iv) Finally, the thermal boundary conditions at the fluid top and bottom (bound to thermal exchanges with the atmosphere, through convection and radiation, and with the ground, through conduction) and the possible thermal insulation due to a superficial crust formation may be considered as well since they affect viscosity and, consequently, propagation velocity (Harris and Rowland, 2009). The cooling process on the fluid top and bottom may induce a phase transition on both sides and lead to the formation of a lava tube (not modelled here).

The mathematical translation of the mass, momentum and energy conservation laws together with conditions (*i–iv*) leads to a system of partial differential equations (PDEs) for which approximated solutions computed by numerical methods are increasingly employed (due to the absence of analytical solutions). However, theoretical models and numerical methods cannot capture the entire complexity of lava properties, and different simplifications have been introduced to speed up codes. Models are distinguished for the deterministic or stochastic approach, the numerical method employed, and the complexity of the physical modelling adopted; hence the associated codes differ in their physical implementations, numerical accuracy, and computational efficiency.

Here we briefly summarize the broad categorization of existing lava flow models, for a detailed review consult (Biagioli, 2021; Hyman et al., 2022): *stochastic models* (DOWNFLOW (Favalli et al., 2005; Tarquini and Favalli, 2011), ELFM (Damiani et al., 2006), VORIS (Felpeto et al., 2007), LASZLO (Bonne et al., 2008), MrLavaLoba (de' Michieli Vitturi and Tarquini, 2021)), *channelled models* (FLOWGO (Harris and Rowland, 2001; Harris et al., 2011; Harris et al., 2015)), *cellular automata models* (MAGFLOW (Bilotta et al., 2012; Del Negro et al., 2008; Ganci et al., 2012; Herault et al., 2009; Vicari et al., 2007), SCIARA (Avolio et al., 2006; Barca et al., 1994; Barca et al., 2004; Crisci et al., 1986; Crisci et al., 1998; Crisci et al., 2008), FLOW FRONT (Wadge et al., 1994; Young and Wadge, 1990), MOLASSES (Connor et al., 2012; Dietterich et al., 2017; Kubanek et al., 2015)), *depth-averaged models* (VOLCFLOW (Kelfoun and Vargas, 2016), Costa and Macedonio (Costa and Macedonio, 2005), ShaLava (Bernabeu et al., 2016), DG LAVA 2D (Conroy and Lev, 2021), LAVA 2D (Hyman et al., 2022)), *nuclear-based models* (CROCO (Michel et al., 2000), MELTSPREAD (Farmer et al., 1990)), *3D models* (LavaSIM (Fujita and Nagai, 2022), GPUSPH (Zago et al., 2019)). The specific approach of our interest is the *depth-averaged* one, which represents an excellent compromise to provide accurate solutions in a reasonable time (since the heavy computational load required by 3D models remains a critical problem), by approximating the full model with a 2D one for the depth-averaged flow variables. This approach relies on the so-called "shallow water approximation" for which the flow depth (the thickness) is required to be much smaller than the horizontal scale of the phenomenon of interest. A small aspect ratio implies that vertical velocities are much smaller than horizontal velocities and can be neglected. Shallow water approximation was first introduced by de Saint-Venant in 1864 and Boussinesq in 1872 (Hager et al., 2019); their original formulation regarded incompressible, isothermal, and non-viscous fluids. However, the classical shallow water model may be enriched by considering viscosity and additional transport equations for energy or temperature and therefore are currently applied to a broader range of geophysical problems for hazard assessment (flood simulations (Coulibaly et al., 2020; Elong et al., 2022), tsunamis propagation (Deb Roy et al., 2007), granular flows such as avalanches, landslides, debris flows, and pyroclastic currents (Fernández-Nieto et al., 2016; Fernández-Nieto et al., 2018; Gueugneau et al., 2021), lava flows). VOLCFLOW (Kelfoun and Vargas, 2016) is an isothermal model that accounts for Bingham-plastic rheology. Instead, Costa and Macedonio (Costa and Macedonio, 2005), ShaLava (Bernabeu et al., 2016), DG_LAVA_2D (Conroy and Lev, 2021), LAVA_2D (Hyman et al., 2022) consider the lava cooling process, the development of different kinds of temperature profiles, a Newtonian (Costa and Macedonio (Costa and Macedonio, 2005)) or Bingham-plastic (all the others) rheology model with different relationships for the temperature-dependent viscosity. Notice that LAVA_2D (Hyman et al., 2022) implements, in addition to complex velocity, temperature and viscosity profiles, the solidification at the ground and the crust formation at the surface.

This paper presents a novel depth-averaged model for lava flows, its validation with some benchmarks for lava flow models established in (Cordonnier et al., 2015) and its application to the real case of Pico do Fogo, Cape Verde, 2014–2015 effusive eruption. In the previous work by some of the authors (Biagioli et al., 2021), a preliminary model has been presented in the broader context of generic viscous fluids by setting the numerical scheme to apply and showing essential results - among which the capability of the model to correctly reproduce the first benchmark of (Cordonnier et al., 2015). The present paper describes how we improved that model by tailoring it for the specific application of lava flows.

As we treat lava as a hot free-surface viscous fluid with heat exchanges with the environment, the present model goes beyond the assumptions of the classic shallow water equations, which are: (*a*) a negligible vertical component of velocity, (*b*) a hydrostatic vertical pressure distribution, (*c*) a constant vertical profile of the horizontal velocity component (which is a consequence of the inviscid flow hypothesis), and (*d*) isothermal fluid. In fact, for viscous fluids, the vertical shear has a significant impact, therefore assumption (*c*) becomes too restrictive and must be relaxed. In addition, for lava flows we overcome even the hypothesis (*d*), whereas the assumptions (*a-b*) remain. We overtake the classic formulation by assuming a viscoplastic model and non-constant vertical profiles for velocity and temperature, which make the model 2.5D. In this way, even if done with strong assumptions on the functional form of the profiles, we describe not only the horizontal variations of the flow variables, but also the variations with depth. By considering the no-slip condition for viscous fluids in contact with surfaces, we consider a parabolic velocity profile. Using a non-constant velocity profile produces a modified momentum equation in which an additional coefficient, known as the *Boussinesq factor* or *shape factor* (Boussinesq, 1877), appears in the advective term. We assume a piece-wise linear vertical profile for the temperature, accounting for the variations near the ground due to conductive heat exchange with the soil. The combined assumptions of non-constant velocity and temperature profiles lead to the appearance of a shape factor inside the advective term of the temperature equation and of some correction factors inside the heat exchange terms. The model has been further enriched by source terms that account for the lava effusion from a circular vent. In conclusion, our model largely respects the requirements (*i–iv*) listed before.

Our governing equations are obtained by integrating the mass, momentum and thermal energy conservation laws over the fluid depth and consist of a system of PDEs. The modifications that we introduced do not change the hyperbolic nature of the equations (see (E. Biagioli, and M. de' Michieli Vitturi, and F. Di Benedetto, 2021)), but, in some cases, they can significantly impact front features and propagation (Hogg and Pritchard, 2004). The spatial discretization method employed is a modified version of the second-order central-upwind scheme introduced by (Kurganov and Petrova, 2007) for the classical shallow water equations, (see (Biagioli et al., 2021)). For the temporal discretization, we use an implicit-explicit Runge-Kutta technique (Russo, 2000; Russo, 2005), which permits an implicit treatment of the stiff terms, such as the viscosity term and thermal heat exchange terms, making the numerical method more efficient.

The paper is organized as follows. First, we present the detailed physical model for lava flow in §2 and suggest the numerical scheme to use. Then, we show and discuss in §3 the results of this model applied to two 2D benchmarks taken from (Cordonnier et al., 2015) and to an actual eruption case, represented by the event that occurred at Pico do Fogo volcano (Cape Verde, 2014–2015). Finally, we present the concluding remarks in §4 and discuss possible further improvements.

2. Method

In this section, we present the physical model we developed and summarize its formal derivation; Table 1 reports all the variables and parameters of the model. More mathematical details about the derivation are available in (Biagioli, 2021).

In this depth-averaged model, we consider lava flows as incompressible and laminar flows over a variable topography of a viscous and homogeneous fluid with Bingham-plastic rheology and temperature-dependent viscosity. Fluid temperature varies because of radiative and convective heat exchanges through the surface with the environment, heat conduction with the ground and viscous heating. The depth-averaged value of density may be constant or vary horizontally, further relaxing the assumptions of the classical shallow water equations, and both the model and the numerical solver retain it in their formalization for this reason. For example, density might depend linearly on temperature, in which case the depth-averaged density depends linearly on the depth-averaged temperature, see (Biagioli et al., 2021) for more details and a related application.

Notice that the laminar flow hypothesis is an important assumption, and that is more suitable for high viscous fluid, precisely when the Reynold number is small ($Re \ll 1$). The laminar regime allows a thermal and rheological stratification, so the core remains hotter than the boundaries, requiring a longer time to cool. On the opposite, turbulent flows see a thermal mixing (unless rheological contrasts inhibit it), and the internal lava cools and solidifies faster than in the laminar case (Griffiths, 2000; Kilburn, 1999).

In this work, we derive the equations by depth-averaging, in the Eulerian framework, the incompressible and 3D formulation of the Navier-Stokes Equations, under the assumption that the horizontal length scale is much greater than the vertical length scale:

$$\frac{\partial \rho}{\partial t} + \nabla\cdot(\rho \mathbf{u}) = 0, \tag{1}$$

$$\frac{\partial (\rho \mathbf{u})}{\partial t} + \nabla\cdot\left(\rho \mathbf{u}\mathbf{u}^T\right) = \rho \mathbf{g} - \nabla p + \nabla\cdot\boldsymbol{\tau}. \tag{2}$$

Eq. (1) is the continuity equation, namely the transport equation for density $\rho(\mathbf{x}, z, t)$, which is advected with velocity $\mathbf{u}(\mathbf{x}, z, t)$, where $\mathbf{x} = (x, y)$. Eq. (2) is the momentum conservation equation, a non-linear partial differential equation that accounts for the velocity advection. Pressure p is the mechanical pressure, which depends on the pressure distribution at the boundary. The viscous stress tensor $\boldsymbol{\tau}(\mathbf{x}, z, t)$ to which we refer here relates to incompressible flows and Newtonian and isotropic fluids with constant viscosity μ. Therefore, according to these assumptions, we get that the viscous stress tensor is defined as $\boldsymbol{\tau} = \mu\left(\nabla\mathbf{u} + (\nabla\mathbf{u})^T\right)$, where $\nabla\mathbf{u}$ is the Jacobian matrix of the velocity field. Because of the incompressible flow condition, that is $\nabla\cdot\mathbf{u} = 0$, we obtain that the term that appears in the momentum equation results as $\nabla\cdot\boldsymbol{\tau} = \mu\Delta\mathbf{u}$ (for these classic arguments, the reader can refer to (Batchelor, 2000)). Since (Biagioli et al., 2021) already present in detail the derivation of the depth-averaged mass and momentum equations, in the present work, we only recall the significant points of those passages.

We adopt a Cartesian coordinates system such that the plane defined by the x and y axes is orthogonal to the z axis, which is parallel, but with opposite verse, to the gravitational acceleration $\mathbf{g} = (0, 0, -g)$ (g approximated by 9.8 $\mathrm{m\,s^{-2}}$). The topography (assumed not to vary with time) is expressed by the function $B(\mathbf{x})$. Assuming that the horizontal length scale is much greater than the vertical length scale and that the vertical dynamics are negligible compared to horizontal effects, the velocity vector $\mathbf{u} = (u, v, w)$ results with $w = 0$. $h(\mathbf{x}, t)$ denotes the fluid thickness above the topography and $\mathscr{T}(\mathbf{x}, z, t)$ is the temperature field. We introduce the notation $\mathbf{U}(\mathbf{x}, t)$ for the z-averaged horizontal velocity vector, whose two components U and V are given by

$$\begin{aligned} U(\mathbf{x},\ t) &= \frac{1}{h}\int_B^{B+h} u(\mathbf{x}, z, t)\, dz, \\ V(\mathbf{x},\ t) &= \frac{1}{h}\int_B^{B+h} v(\mathbf{x}, z, t)\, dz. \end{aligned} \tag{3}$$

Similarly, T is the notation for the depth-averaged temperature

$$T(\mathbf{x}, t) = \frac{1}{h}\int_B^{B+h} \mathscr{T}(\mathbf{x}, z, t)\, dz. \tag{4}$$

Under the assumptions of laminar flow and viscous fluid, a vertical velocity profile develops satisfying the conditions of (*i*) null velocity at the bottom, (*ii*) null traction between air and fluid, and (*iii*) maximum speed at the free surface. Also, considering the motion of a Newtonian fully developed laminar viscous flow (with constant viscosity along the

Table 1
Variables and parameters of the model.

Symbol	Definition	Unit
ρ	density	$\mathrm{kg\,m^{-3}}$
h	fluid thickness	m
$\mathbf{U} = (U, V)$	depth-averaged velocity	$\mathrm{m\,s^{-1}}$
T	depth-averaged temperature	K
R	volume rate of fluid per unit area	$\mathrm{m\,s^{-1}}$
g	gravity	$\mathrm{kg\,m\,s^{-2}}$
B	topography elevation	m
T_{ref}	reference temperature	K
T_{vent}	temperature at the vent	K
T_{soil}	invariable soil temperature	K
c_p	fluid specific heat	$\mathrm{m^{-2}\,s^{-2}\,K^{-1}}$
k_{fl}, k_{soil}	fluid and soil th. conductivity	$\mathrm{W\,m^{-1}\,K^{-1}}$
n	param. for fluid thermal boundary layer	–
M	param. for soil thermal boundary layer	–
κ	fluid th. diffusivity	$\mathrm{m^2\,s^{-1}}$
$\mathscr{H}$	conductive coefficient	$\mathrm{m\,s^{-1}}$
λ	heat transfer coefficient	$\mathrm{W\,m^{-2}\,K^{-1}}$
f	exposed inner core fractional area	–
$\mathscr{W}$	convective coefficient	$\mathrm{m\,s^{-1}}$
ε	emissivity	–
σ_{SB}	Stefan-Boltzmann constant	$\mathrm{W\,m^{-2}\,K^{-4}}$
$\mathscr{E}$	radiative coefficient	$\mathrm{m\,s^{-1}\,K^{-3}}$
$\mathscr{Z}$	viscous heating coefficient	$\mathrm{m^{-2}\,s^2\,K}$
ζ, ψ	temperature source terms coefficients	–
γ	friction coefficient	$\mathrm{m\,s^{-1}}$
μ	dynamic viscosity	Pa s
$\tilde{\mu}$	power-law viscosity	Pa s
τ_0	yield stress	Pa
b	rheological parameter	$\mathrm{K^{-1}}$
μ_{ref}	dynamic viscosity at T_{ref}	Pa s

vertical direction), the balance of friction and gravitational force leads to a parabolic velocity profile, as represented in Fig. 1a, similar to a Poiseuille flow (Dragoni et al., 2005). Notice that this profile develops for both velocity components $\mathbf{u} = (u, v)$.

From the previous conditions, the following relationship between $\mathbf{u}$ and $\mathbf{U}$ may be deduced:

$$\mathbf{u}(\mathbf{x}, z, t) = \frac{3}{2}\left\{1 - \left[\frac{B(\mathbf{x}) + h(\mathbf{x}, t) - z}{h(\mathbf{x}, t)}\right]^2\right\}\mathbf{U}(\mathbf{x}, t). \tag{5}$$

Therefore, by using the assumptions of parabolic profile ($i - iii$), we get an explicit expression of the vertical distribution $\mathbf{u}(z)$ in terms of $\mathbf{U}$ and the relative vertical position.

The *depth-averaged continuity equation* is derived by integrating the mass conservation equation, Eq. (1), over the flow thickness, and it results as follows:

$$\frac{\partial(\rho h)}{\partial t} + \nabla\cdot(\rho h\mathbf{U}) = 0. \tag{6}$$

The *depth-averaged momentum conservation equations* is obtained by depth integrating the momentum conservation equation, Eq. (2), and assuming a hydrostatic profile for pressure p, i.e. $\partial_z p(\mathbf{x}, z, t) = -\rho(\mathbf{x}, t)g$:

$$\frac{\partial(\rho h\mathbf{U})}{\partial t} + \nabla\cdot\left(\beta_u \rho h\mathbf{U}\mathbf{U}^T\right) + \nabla\left(\frac{1}{2}\rho g h^2\right) = -\rho g h\nabla B - \rho\gamma\mathbf{U}. \tag{7}$$

The differences between Eqs. (6–7) and the classical shallow-water equations are the viscous term $-\rho\gamma U$ and the coefficient β_u. We remark that, in obtaining Eqs. (6–7) by an integration over the flow depth, we neglected the vertical variations of density (which, for a lava flow, are small), but we kept the density in the equations because of the possible variations with time and with the horizontal coordinates, which can occur on longer time scales.

The coefficient β_u is known in the literature as *Boussinesq momentum coefficient* or *shape factor* or *corrector factor*; in general, its magnitude relates the mean square velocity to the square of the mean velocity, reflects the shear in the profile of the horizontal fluid velocity, and may depend on factors such as the Reynolds number or the boundary roughness. Even though the value of β_u is frequently set equal to unity (which holds only when velocity is constant over the flow thickness), it is well known that this coefficient may have a significant effect on the dynamics of the flow when a complete sheared flow is expected (Hogg and Pritchard, 2004). The presence of this coefficient in the momentum equation is due to the nonlinearity of the advective term with respect to the velocity (indeed, the term $\nabla\cdot(\rho\mathbf{u}\mathbf{u}^T)$ in Eq. (2) is quadratic in $\mathbf{u}$, whereas $\nabla\cdot(\rho\mathbf{u})$ in Eq. (1) is linear). In case of parabolic velocity profile, as represented in Eq. (5), by depth-averaging the momentum equation, Eq. (2), we obtain that the value of the Boussinesq coefficient is $\beta_u = 6/5$ (but different velocity profiles, for example, when non-Newtonian viscosity is considered, will result in different values of β_u). For the detailed derivation of the value $\beta_u = 6/5$ we refer the reader to (Biagioli, 2021).

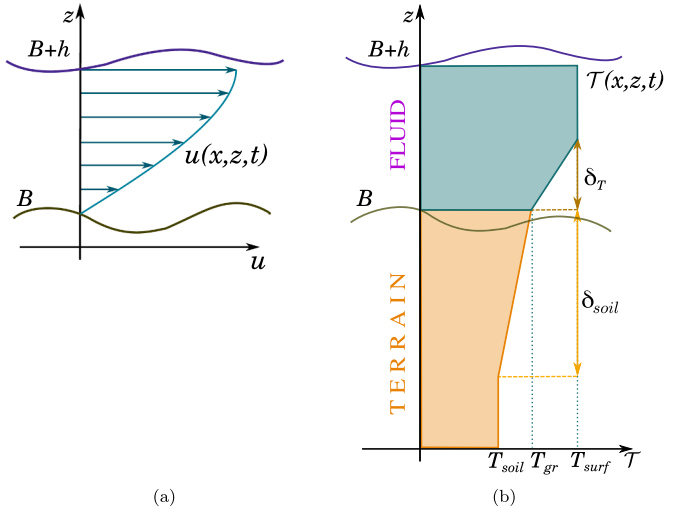

Fig. 1. Vertical profiles assumed in the model. (a) Parabolic velocity profile. (b) Piecewise-linear temperature profile; δ_T and δ_{soil} are the thermal boundary layers of fluid and terrain, respectively.

Following (Costa and Macedonio, 2005), the friction term is given by $-\rho\gamma\mathbf{U}$, where the friction coefficient expresses as $\gamma := 3\mu/(h\rho)$ due to the parabolic velocity profile. Such a coefficient is inversely proportional to the fluid thickness and directly proportional to the viscosity, which coincides with the dynamic viscosity in the Newtonian case. In the case of a Bingham plastic rheology, the friction coefficient slightly changes its expression, resulting in

$$\gamma := \frac{3}{h\rho}\widetilde{\mu} + \frac{\tau_0}{\rho|U|}. \tag{8}$$

In this equation, $\widetilde{\mu}$ is the power-law viscosity (also called flow consistency index) that Herschel and Bulkley introduced in 1926 to express the shear stress as a function of the shear rate for both Newtonian and non-Newtonian fluids (Tang and Kalyon, 2004). τ_0 is the yield stress and is a threshold for the shear stress: if the shear stress magnitude is smaller than that, namely when $|\boldsymbol{\tau}| < \tau_0$, then there is no deformation. Bingham fluids are characterized by $\tau_0 > 0$ and Newtonian fluids by $\tau_0 = 0$. Notice also that when one uses the Bingham plastic rheology (Eq. (8)), if the velocity in the momentum equation (Eq. (7)) goes to zero, the friction term does not go to zero because of the velocity at the denominator in the yield stress term. For a Bingham fluid, plugged flow can occur far from the bottom, where the shear stress is smaller, and the velocity becomes constant with depth (Tallarico and Dragoni, 2000). This results in a deviation from the assumed parabolic profile, which is not considered here.

For several materials, the viscosity, be it dynamic μ or power-law $\widetilde{\mu}$, is strongly temperature dependent, and in the case of lava, the simple Nahme's exponential relationship between viscosity and temperature may be assumed (Costa and Macedonio, 2002):

$$\widetilde{\mu} = \mu_{ref} e^{-b\left(T - T_{ref}\right)}, \tag{9}$$

where b is an appropriate rheological parameter and μ_{ref} is the viscosity at a particular reference temperature T_{ref} that may be, for instance, the emission temperature at the vent T_{vent}. In the present work, we implicitly assume the crystallinity-dependence of viscosity through the value of the rheological parameter b; in fact, we do not have either equations or terms describing the crystallization process explicitly.

2.1. Temperature profile for soil conduction and heat exchanges

Because of the dependence of viscosity on temperature, we introduce an additional equation describing the temperature evolution. Although the temperature equation usually is derived from the energy conservation law (written in terms of the temperature), we consider the temperature only as a transported quantity. In the following, we derive the depth-averaged equation, which accounts for the transport of the temperature $\mathcal{T}$, the heat exchange phenomena through convection and radiation with the environment and conduction with the ground, and the viscous heating. The result is a transport equation containing the advection term of the depth-averaged temperature and presenting source terms related to radiation, convection and viscous heating. We stress that depth-averaged variables are chosen as the unknowns of the system of equations: in particular, the temperature will appear in the average form T so that some independent quantities will be expressed in terms of T (even though this may seem counterintuitive).

We assume that the vertical temperature variations are due to the conductive heat flux between the fluid and the ground with the consequent development of two thermal boundary layers in both materials.

Indeed, in the case of lava flows or similar situations, the terrain is colder than the fluid, so a thermal boundary layer emerges in the fluid. At the same time, the ground temperature increases to a certain depth because of the presence of the hotter fluid, hence an underground thermal boundary layer develops too. By succeeding in doing so, we can describe the heat exchange processes in terms of the fluid depth-averaged temperature and the unchanged temperature deep underground.

We make two hypotheses to model heat conduction: (i) the fluid and the ground are both homogeneous and isotropic materials, and their thermodynamic properties are temperature independent, (ii) the time scale of the thermal diffusion process is faster than the time scale of the boundary conditions changes, so we can assume an equilibrium condition (namely, the temperature profile instantaneously reaches the thermal equilibrium). The latter assumption is justified by field and theoretical studies of lava flows showing that the interface temperature between the flow and the underlying ground rapidly reaches approximately the halfway point between the relatively low original ground temperature and the high lava melt temperature (Davies, 2007; Turcotte and Shubert, 1982).

Because of assumption (i), the fluid and ground thermal conductivity, named k_{fl} and k_{soil}, respectively, are constant and do not depend on temperature. On the other hand, thanks to assumption (ii), we may refer to the heat equation at the stationary state condition (namely to the Laplace equation) restricted to the vertical direction, leading to a linear solution:

$$\mathscr{T}(z) = Cz + D.$$

This leads to a linear profile in each thermal boundary layer considered. Consequently, the overall temperature profile is piecewise-linear. We denote with δ_T and δ_{soil} the thermal boundary layer thicknesses of the fluid and soil, respectively. T_{surf} is the temperature of the fluid free-surface, T_{gr} is the temperature at the fluid/ground interface, and T_{soil} is the unchanged temperature underground, see Fig. 2. The profile's explicit expression is:

$$\mathscr{T}(\mathbf{x},z,t) = \begin{cases} T_{surf}(\mathbf{x},t), & \text{if } B+\delta_T < z \le B+h \\ \dfrac{T_{surf}(\mathbf{x},t) - T_{gr}(\mathbf{x},t)}{\delta_T}(z-B) + T_{gr}(\mathbf{x},t), & \text{if } B < z \le B+\delta_T \\ \dfrac{T_{gr}(\mathbf{x},t) - T_{soil}}{\delta_{soil}}[z-(B-\delta_{soil})] + T_{soil}, & \text{if } B-\delta_{soil} < z \le B \\ T_{soil}, & \text{if } z \le B-\delta_{soil}. \end{cases} \tag{10}$$

Usually, the thickness of the fluid thermal boundary layer is approximated as a fraction of the whole flow depth, so $\delta_T = h/n$ (with $n \ge 1$) (Costa and Macedonio, 2005). Likewise, even the thickness of the ground boundary layer depends on the fluid depth, but with a different relationship: $\delta_{soil} = Mh$ (with $M \ge 1$); for example, in (Patrick et al., 2004), focused on the characterization of the cooling of a stationary lava flow, the authors use $M = 2$. We observe that the introduction of a vertical temperature profile also leads to a viscosity profile because of the dependence of the viscosity on the temperature (see Eq. 9). In the model presented here, we neglect the effect of these viscosity vertical changes on developing a parabolic velocity profile by using an average viscosity value obtained from the depth-averaged temperature value.

According to the definition of the depth-averaged temperature T, Eq. (4), we integrate on the depth the temperature by using the expression of its profile, Eq. (10), and obtain a relation binding T to the top and bottom fluid temperatures, namely, T_{surf} and T_{gr}, and to the thickness index n:

$$T = \left(1 - \frac{1}{2n}\right) T_{surf} + \frac{1}{2n} T_{gr}. \tag{11}$$

The Fourier law (consult (Fagents et al., 2012)) states that the conductive flux q_{cond} along the vertical direction, intended as the heat flux through a unit area per unit of time, is linearly proportional to the negative temperature gradient and to the thermal conductivity k. By assuming the same heat flux in both the fluid and solid, the following equality holds

$$q_{cond}^{(fl)} = -k_{fl}\frac{T_{surf} - T_{gr}}{\delta_T} = -k_{soil}\frac{T_{gr} - T_{soil}}{\delta_{soil}} = q_{cond}^{(soil)}. \tag{12}$$

By rearranging the previous equation, we express T_{gr} in terms of the surface and soil temperatures

$$T_{gr} = (1-\phi)T_{surf} + \phi T_{soil}, \text{ with } \phi := \frac{1}{\frac{k_{fl}}{k_{soil}} nM + 1}. \tag{13}$$

Using the depth-averaged model, we need to express the surface and ground temperature, T_{surf} and T_{gr}, in terms of the depth-averaged and soil temperatures, T and T_{soil}, in order to close the system of equations. So, from the previous equations Eq. (11) and Eq. (13), and after some manipulation, we find the expressions that we need:

$$T_{surf} = \zeta T + (1-\zeta)T_{soil}, \quad \text{with } \zeta := \frac{1}{1 - \phi/(2n)}, \tag{14}$$

$$T_{gr} = \psi T + (1-\psi)T_{soil}, \quad \text{with } \psi := (1-\phi)\zeta. \tag{15}$$

We also notice that when $n \to +\infty$ then ζ and ψ go to 1, consequently $T_{surf} \approx T$ (from Eq. (14)) and $T_{gr} \approx T$ (from Eq. (15)).

In the following, we describe the advective and source terms of the transport equation for T.

2.1.1. Advective term

We integrate the advective term of the temperature equation over the fluid depth by using the explicit expressions of velocity and temperature profiles, Eqs. (5, 10), obtaining the next expression:

$$\int_B^{B+h} \mathscr{T}(z)\mathbf{u}(z)dz = h\mathbf{U}\left[(1-\theta)T_{surf} + \theta T_{gr}\right], \text{with } \theta := \frac{4n-1}{8n^3}. \tag{16}$$

By writing T_{surf} and T_{gr} in terms of T and T_{soil} through Eqs. (14, 15), the temporal and advective terms integrated over the fluid depth result as:

$$\frac{\partial(hT)}{\partial t} + \nabla\cdot\{h\mathbf{U}[T + (\beta_T - 1)(T - T_{soil})]\}, \text{with } \beta_T := \theta(\psi - \zeta) + \zeta. \tag{17}$$

To express the dependence of β_T on the physical quantities, we replace the definitions of $\phi, \theta, \psi, \zeta$ using Eqs. (14, 15, 16):

$$\beta_T = 1 + \frac{k_{soil}(2n-1)^2}{4n^2\left[2n^2 M k_{fl} + (2n-1)k_{soil}\right]}. \tag{18}$$

The value of β_T is clearly greater than 1 because the fraction has positive factors (remember that $n \ge 1$). Because of this, and since $T - T_{soil} > 0$, the temperature advected (that is written in the square brackets of Eq. (17)) is surely greater than the average temperature T. Therefore models that advect only the depth-averaged temperature underestimate this flux.

From the explicit expression of β_T, we notice that the soil temperature influence becomes negligible and that the vertical distribution of temperature arises similar to a constant vertical profile in two situations: when the thickness $\delta_T = h/n$ of the fluid thermal boundary layer thins or when the thickness $\delta_{soil} = Mh$ of the soil thermal boundary layer increases a lot. In fact, as n or M goes to $+\infty$, the value of β_T goes to 1 so that the advective term reduces to $\nabla\cdot(h\mathbf{T}\mathbf{U})$, which is the classic expression of the depth-averaged equation obtained under the assumption of a uniform temperature profile (namely $T = T_{surf} = T_{gr}$). The value, and hence the impact, of β_T depends on the thermophysical properties of lava and soil (thermal conductivity k_{fl}, k_{soil}) and the parameters that model the thermal profile (n, M). In realistic lava flows scenario, the value of these parameters might be $n = 2$, $M = 2$ (Patrick et al., 2004), $k_{fl} = 2.0$ for basaltic lava (Costa and Macedonio, 2005), and $k_{soil} = 0.83$ which is a mean value for soil (Darkwa et al., 2013) The

resulting value is $\beta_T \approx 1.01$, so the influence of the profile on the advective term is very small.

2.1.2. Conductive heat transfer source term

So far, we have analyzed how conductive heat loss affects the temperature profile and have derived a consequent expression for the advective flux. However, we must also quantify the actual thermal loss due to conduction and write the corresponding source term. The Fourier Law in Eq. (12) states that the heat exchange between the hot fluid and cold ground is directly proportional to the temperature gradient and the thermal conductivity. Since we are deriving an equation for temperature and not for energy, we divide the thermal conductivity by the specific heat c_p and density ρ, thus the thermal diffusivity, defined as $\kappa k_{fl}/(\rho c_p)$, appears:

$$\frac{q_{cond}}{\rho c_p} = -\kappa \frac{T_{surf} - T_{gr}}{\delta_T} \quad . \tag{19}$$

Considering Eqs. (14, 15) to express the surface and ground temperature in terms of T and T_{soil} and rearranging the terms, we get the final expression of the conductive heat loss term:

$$\mathscr{S}_{cond} = -\mathscr{H}(\zeta - \psi)(T - T_{soil}), \text{with } \mathscr{H} := \kappa n/h. \tag{20}$$

2.1.3. Convective heat transfer source term

Convection heat loss is the heat transfer from the surface of a warm body to the surrounding colder gas or liquid and is characterized by the motion of such fluid. In our case, the warm body corresponds to the free surface of the hot lava, overhung by the colder air. In models where the air is not represented (as in the present case) or when the whole complexity of the processes is not properly accounted for, there is no exact modelling of the convective phenomenon. However, the convective heat flux can be described by the Newton law of cooling in terms of the heat transfer coefficient λ and of the temperature difference between the fluid surface and the environment (Fagents et al., 2012), and writes as follows:

$$q_{conv} = \lambda f \left[T_{surf} - T_{env}\right], \tag{21}$$

where T_{env} denotes the constant environmental temperature. The coefficient λ depends on the physical properties of the colder fluid. Moreover, the value of λ changes if one models natural or forced convection, for example, a value between 2.5 and 25 $\mathrm{Wm^{-2}K^{-1}}$ is proposed in the literature (Kosky et al., 2013) for natural air convection and between 10 and 500 $\mathrm{Wm^{-2}K^{-1}}$ for the forced case, as in the presence of wind. The variable f indicates the fractional area of the exposed inner core: the value of f is exactly equal to 1 for a fluid completely molten; when there is a superficial crust that insulates partially or totally the fluid, as it might happen in the case of lava (consult (Fagents et al., 2012) for more details) f assumes a smaller value. Moreover, in natural flows, the value of f may change with time and space because it depends on the solidification temperature of the material considered and on its chemical composition. In this model, we assume, for simplicity, a constant value for f.

By using the same argument as for conduction, we divide the coefficient in Eq. (21) by the specific heat c_p and density ρ, express T_{surf} in terms of T and T_{soil} (Eq. (14)), and obtain the convective heat transfer source term to add to the temperature equation:

$$\mathscr{S}_{conv} = \frac{q_{conv}}{\rho c_p} = -\mathscr{W}[\zeta T + (1-\zeta)T_{soil} - T_{env}], \text{with } \mathscr{W} := \frac{\lambda f}{\rho c_p}. \tag{22}$$

2.1.4. Thermal radiation transfer source term

The so-called Stefan-Boltzmann law describes the radiative heat flux, stating that the rate of thermal radiation emitted from a surface per unit area q_{rad} is:

$$q_{rad} = \varepsilon \sigma_{SB} T_{surf}^4, \tag{23}$$

namely is proportional to the fourth power of its absolute temperature at the surface, i.e. T_{surf}, expressed in kelvin, to the Stefan-Boltzmann constant $\sigma_{SB} = 5.67{\cdot}10^{-8}\ \mathrm{Wm^{-2}K^{-4}}$ and to the emissivity ε of the material, for more details see (Modest, 1993). Our model accounts for the radiative heat exchange between the fluid and the environment, so the radiative heat flux depends on the difference of the fourth powers of the surface temperature and environmental temperature, according to Eq. (23), and consequently the radiative heat loss of the fluid is

$$-\varepsilon \sigma_{SB} f \left[T_{surf}^4 - T_{env}^4\right]$$

where ε is the fluid emissivity. The parameter f of the fractional area of the exposed inner core appears even in this term because the radiative heat loss is influenced by the presence of a superficial crust as well.

By using the same argument as for conduction, we divide the heat loss by the specific heat c_p and density ρ, express the surface temperature in terms of T and T_{soil} (Eq. (14)), and finally get the expression for the radiative term to add in the transport equation:

$$\mathscr{S}_{rad} = -\mathscr{E}\left[(\zeta T + (1-\zeta)T_{soil})^4 - T_{env}^4\right], \text{with } \mathscr{E} := \frac{\varepsilon \sigma_{SB} f}{\rho c_p}. \tag{24}$$

2.2. Further considerations

(a) In the case that a constant velocity profile is assumed, namely when $u(z) = U$ as in the classic formulation of the shallow-water equations, a thermal boundary layer may still develop. The consequence is a simplification in the advective term, and the equation results as follows:

$$\frac{\partial(hT)}{\partial t} + \nabla\cdot(hT\mathbf{U}) = \mathscr{S}_{cond} + \mathscr{S}_{conv} + \mathscr{S}_{rad} \tag{25}$$

(b) We discuss the asymptotic behaviour of the thermal exchange terms. Concerning the convective and radiative terms, Eqs. (22, 24), the limit case of a constant temperature profile within the lava flow is studied, corresponding to a negligible lava thermal boundary layer ($n \to \infty$). One observes that both terms contain the parameter ζ that multiplies T, and that, according to (14), $\zeta \to 1$ when $n \to \infty$. We get that the convective and radiative terms tend to $-\mathscr{W}(T - T_{env})$ and $-\mathscr{E}(T^4 - T_{env}^4)$ respectively, and these expressions correspond to those reported in (Costa and Macedonio, 2005).

(c) When the thermal boundary layer in the soil is not accounted for in the modelling derivation procedure, then $T_{gr} = T_{soil}$, and this coincides with the model proposed in (Costa and Macedonio, 2005). In such a circumstance, our conductive term is still described by Eq. (19) as $\kappa(T_{surf} - T_{gr})/\delta_T$, instead of that present in (Costa and Macedonio, 2005) that is $\kappa(T - T_{gr})/\delta_T$. When the difference between T and T_{surf} is small, replacing T_{surf} by T is a little underestimation and, from this approximation, the different expression may be deduced.

(d) A shrewdness must be accounted for in a simulation where a source area representing a vent is present. At the vent, there is no cooling at the bottom because there is no conductive heat exchange as the ground is the magma rising in the conduit. For this reason, the temperature profile is constant in the source area. It comes out that the advective flux term assumes the expression as follows and that only the heat exchanges with the air must be considered:

$$\frac{\partial(hT)}{\partial t} + \nabla\cdot(hT\mathbf{U}) = -\mathscr{W}(T - T_{env}) - \mathscr{E}(T^4 - T_{env}^4).$$

2.2.1. Viscous heating term

In the dynamics of fluids characterized by a temperature-dependent viscosity, the coupling between the momentum and temperature (or energy) equations is essential. We obtain such coupling by assuming Nahme's exponential law of Eq. (9) and including the viscous heating, another significant process that connects temperature to dynamics. For

viscous fluids, such as lava or polymers, the viscous friction increases the fluid temperature where viscosity is higher, namely near the surfaces touched by the fluid: for example, in an open-channel flow the increase of temperature happens near the bottom, instead for a fluid in a pipe occurs near the tube walls. The temperature increment leads to a viscosity decrease, which reflects in a velocity increase, and then the higher velocity causes further heating. Moreover, viscous heating may change the velocity and temperature profiles, for example, transforming a parabolic velocity profile into a constant velocity profile. This may happen in the case of an open-channel flow, which presents the profile of Fig. 1a, as well as in the case of a flow in a natural or artificial conduit, which develops a slightly different profile, see (Kauahikaua et al., 1998). In the depth-averaged model introduced here, we derive a source term for the viscous heating by depth-averaging the term presented in (Costa and Macedonio, 2003), which states that the viscous heating is proportional to the dynamic viscosity and the square of the vertical derivative of velocity:

$$\frac{1}{\rho c_p}\int_B^{B+h}\mu\left[\left(\frac{\partial u}{\partial z}\right)^2+\left(\frac{\partial v}{\partial z}\right)^2\right]dz=\mathscr{Z}\gamma\left(U^2+V^2\right),\quad \mathscr{Z}:=\frac{1}{c_p}; \tag{26}$$

for details see (Biagioli, 2021). We point out that if we had assumed a velocity boundary layer of thickness $\delta_u = h/\alpha$ with a parabolic profile, we would have found $\mathscr{Z} = \alpha/c_p$, instead we have simply $\alpha = 1$.

2.3. Synthesis and numerical schemes

We write the results obtained previously all together in a system of equations with an additional source term R accounting for new material release, such as lava exiting from a volcanic vent, at the emission temperature T_{vent} into the system at the volumetric rate of fluid per unit area. Consequently, additional source terms are added to the continuity and temperature equations, whereas no "vent" term is in the momentum equations because we assume that fluid exits with no velocity along x and y.

$$\frac{\partial(\rho h)}{\partial t}+\nabla\cdot(\rho h\mathbf{U})=\rho R, \tag{27a}$$

$$\frac{\partial(\rho h\mathbf{U})}{\partial t}+\nabla\cdot\left(\beta_u\rho h\mathbf{U}\mathbf{U}^T\right)+\nabla\left(\frac{1}{2}\rho g h^2\right)=-\rho g h\nabla B-\rho\gamma\mathbf{U}, \tag{27b}$$

$$\begin{aligned}&\frac{\partial(hT)}{\partial t}+\nabla\cdot\{[T+(\beta_T-1)(T-T_{soil})]h\mathbf{U}\}\\&=\mathscr{S}_{cond}+\mathscr{S}_{conv}+\mathscr{S}_{rad}+\mathscr{Z}\gamma\mathbf{U}^T\mathbf{U}+RT_{vent}.\end{aligned} \tag{27c}$$

Notice that $\mathbf{U}$ is a column vector, so Eq. (27b) consists of two scalar equations. For Newtonian fluids, the friction coefficient is $\gamma := 3\mu/(h\rho)$. Whereas, in the case of the Bingham plastic model, the system couples with the constitutive Eq. (8) for the friction coefficient expression. Also, Nahme's relationship holds for a temperature-dependent viscosity, Eq. (9), and the presence of $b \neq 0$ produces a coupling between the momentum and temperature equations. Table 1 summarizes all the relevant variables and parameters introduced in our model.

Concerning the analytical properties of the system of Eqs. (27), the study of the system's hyperbolicity and the role of the shape parameters are detailed in (Biagioli et al., 2021). In light of the hyperbolic character of equations, classical numerical techniques developed for such kinds of equations (LeVeque, 2002; Toro, 1990) apply to solve them. We describe below the numerical approach used to approximate the system's solution, whose details are reported in (Biagioli, 2021; Biagioli et al., 2021; de' Michieli Vitturi et al., 2019).

The spatial discretization scheme is a modified version of a central-upwind scheme introduced in (Kurganov and Petrova, 2007), which belongs to the family of Finite Volume Methods. It is a second-order scheme when applied with the use of flux limiters. This allows the creation and propagation of discontinuities in the solutions and enforces the conservation properties of the equations. As proved in (Biagioli et al., 2021), this scheme respects the so-called *well-balancing* property, as it preserves the *stationary steady states* that, in our case, consist of the *lake-at-rest* conditions, namely a horizontal free surface with zero velocity, constant temperature, no emission of new fluid in the system and no heat exchanges with the environment. Moreover, the scheme guarantees the *non-negativity* of the fluid depth h throughout the simulation, respecting the so-called *positivity preserving* property.

The time discretization scheme uses an Implicit-Explicit Runge-Kutta method as described in (Pareschi and Russo, 2000). We implicitly treat the stiff terms, namely the friction term of the momentum equation and the conductive, convective and radiative terms of the temperature equation. The other terms, i.e., the flux terms, the pressure term in the momentum equation, the viscous heating term in the temperature equation and the remaining source terms, are treated explicitly.

Despite the simplifications introduced with the shallow water approach, the depth-averaged models have proven to be accurate enough to be a more convenient choice, and the advantage of a meagre computational cost increases the convenience of this choice with respect to 3D models. Indeed, one of the benefits of the depth-averaged approach is that the viscous term is not modelled through a second-order differential term but through a simpler and non-differential term. The implicit treatment of the viscous forces for 3D models in the numerical discretization would require the solution of a large coupled system of equations resulting from the implicit spatial discretization of the second-order differential term, for this reason, some 3D models rely on a simpler semi-implicit treatment of the viscous term (Bilotta et al., 2022). Instead, in depth-averaged models, there is no coupling between the equations associated with these terms. This allowed us to adopt the IMEX scheme, where the implicit terms are integrated cell by cell, significantly reducing the complexity of the problem.

The following numerical scheme properties refer to the model description and terminology presented in (Biagioli, 2021; Biagioli et al., 2021; de' Michieli Vitturi et al., 2019). In order to preserve the solution positivity and the explicit scheme stability associated with the CFL condition, a variable time step is used, which has been set (in terms of the spatial discretization steps) to the following values:

$$\Delta t = k\,\min\left\{\frac{\Delta x}{a},\ \frac{\Delta y}{b}\right\}\ \text{for the 2D simulations, with } k = 0.24, \tag{28}$$

where a, b are the maximum local propagation speeds at interfaces defined in (Kurganov and Petrova, 2007, Theorem 3.1). In each test we present here, the generalized minmod limiter (with $\theta = 1.3$) is adopted because it is proved to produce very accurate solutions (Biagioli et al., 2021). We use the 2-stage IMEX R-K scheme for the time marching (Pareschi and Russo, 2000). We set the initial time-step as $\Delta t = 10^{-4}$ s and use open boundary conditions, which means imposing zero-gradient Neumann conditions both for velocities, free surface $h + B$ and temperature. In the upcoming tests, we compare simulations obtained with computational grids of coarse and finer resolutions, where the grid is refined by halving the discretization step. This means that, for 2D cases like ours, the number of cells obtained with the refinement is four times the previous number and that the time step must also be halved to continue to meet the CFL condition, Eq. (28). Consequently, the computational cost increases by eight times.

3. Applications

The Fortran 90 numerical code developed for this work (available at (Biagioli and de' Michieli Vitturi, 2021)) is based on the solver described in (de' Michieli Vitturi et al., 2023). It has been tested and validated by some literature cases in (Biagioli et al., 2021) where a preliminary temperature model was developed. (Biagioli et al., 2021) also investigated the role of the correction factors. Two 1D tests that perform a dam-break (over a horizontal and an inclined plane, respectively) were

presented, and they showed that the influence of the velocity corrector factor is non-negligible in the presence of supercritical flows, i.e. when the inertial force has a dominant effect on the gravitational force. This condition is verified when the Froude number is greater than 1, where the Froude number is defined as $Fr = |\mathbf{U}|/\sqrt{gh}$. In particular, the simulations that account for the parabolic velocity profile are initially slower than the ones with the constant profile, but after there is an overtake and they subsequently propagate faster. (Biagioli et al, 2021) also presented the 2D simulation of a warm fluid (with a temperature-dependent viscosity), initially concentrated on the top of an inclined plane and then slid down over it. In such a test, the impact of the temperature profile correction factor was tested, proving that its influence is not only not negligible but significantly impacts the thickness distribution and the front position. As already stated, the temperature model adopted in (Biagioli et al., 2021) slightly differs from the one presented in this paper as it doesn't account for the thermal exchanges, having been created to consider only the advection of temperature with a vertical profile. Anyway, the observations from the 2D simulations performed there give an idea about the non-negligible impact of the corrector factors. Indeed, when the piecewise linear temperature profile is considered, due to the combination of velocity and thermal profiles, the top layer has the highest temperature and moves faster than the lower layer. As the top layer propagates faster, it arrives to constitute the front and leads to a further front extent. Meanwhile, the fluid that remains behind becomes, on average, colder as mainly constituted by the lower layer. In this situation, the depth-averaged temperature of the fluid that remains behind decreases, leading to a higher viscosity and, therefore, the fluid there moves slower. Bringing the discussion of this process into the case of the simulation on the inclined plane, it results that the fluid that remains behind is the one that occupies the upper part of the inclined plane, and as a consequence, it tends to accumulate, constituting a pile. Conversely, in the case of a constant thermal profile, the pile does not form.

In the previous work (Biagioli et al., 2021), we mostly focused on 1D tests, instead, in the present paper, we continue the validation exclusively by 2D simulations. The tests' order is of increasing complexity to highlight the single performances of each implemented feature, such as the temperature evolution, the Bingham plastic temperature-dependent viscosity, and the use of a real volcano topography with realistic parameters.

The first two tests presented originate from (Cordonnier et al., 2015), which proposes a suite of benchmark tests for lava flow models, and they have been combined in (Biagioli et al., 2021) with another benchmark given (dam-break of a viscous fluid over a flat bottom) to complete the validation for the 1D case. The first test (§3.1) consists of the spreading of an isothermal viscous fluid over an inclined plane with the aim of checking the fluid spreading correctness with respect to three directions. The second test (§3.2) treats the spreading from a source, over a flat plane, of a hot viscous fluid that cools during the axisymmetric propagation because of radiative, convective and conductive heat loss. For this test, viscosity is not temperature-dependent, hence the dynamics are not influenced by that. The aim of the test is to check both the fluid propagation and temperature changes. The third and last test (§3.3) is the simulation of a real lava flow in the context of a realistic effusive eruption, hence we modelled a Bingham plastic hot fluid and we accounted for the thermal heat exchanges with the environment and soil, the temperature-dependent viscosity, and the viscous heating. We simulate the early 24 h of the Fogo eruption that occurred in 2014–2015 to study the sensitivity of model solutions to the rheological parameters and to the position of the vents. For all the tests presented in this work, we assumed a constant density because of the negligible variations in temperature and/or density. This assumption is valid for both the laboratory experiments, performed with viscous fluids whose density does not change during the test execution, and for the Fogo eruption, for which the density changes are negligible in the 24 h simulated.

A classical comparison between simulation results and laboratory data, analytic data and real data is often based on comparing the extent of the flows. Besides this kind of analysis, this work also presents results showing the fluid thickness, viscosity, and temperature.

3.1. Inclined viscous isothermal spreading

This test origins from a laboratory experiment of silicon oil spreading on an inclined plane of slope α, injected through a point hole at a constant flow rate R, as represented in Fig. S1 (Supplementary Material §S.1). (Lister, 1992) used this laboratory experiment and derived some asymptotic scaling behaviours to analyze his numerical model's performance. Similarly, we aim to compare our results with his and the laboratory experiment. The set-up parameters we have employed follow those used by (Lister, 1992): the source point has a circular area with radius $r = 10^{-3}$ m, the plane is inclined at a slope of $\alpha = 2.5^{\circ}$ from the horizontal direction, the fluid supply rate is $1.48{\cdot}10^{-6}\,\mathrm{m^3\,s^{-1}}$ and the kinematic viscosity ($\nu := \mu/\rho$) is $\nu = 11.3{\cdot}10^{-4}\,\mathrm{m^2\,s^{-1}}$; a Newtonian viscosity is assumed and no thermal phenomena are accounted for.

A rectangular computational domain $[-35\,\mathrm{cm},\ 115\,\mathrm{cm}] \times [-45\,\mathrm{cm},\ 45\,\mathrm{cm}]$ is created and discretized by two grids of different resolutions, a coarse one with 150×90 cells (low resolution) and a finer one with 300×180 cells (high resolution). In every plot reported, we show only values of the thickness h greater than 10^{-3} m, which is rather reasonable since they correspond to the 95% of the total values computed.

Figure 2 reports the flow contours as a function of time. On the left, the results coming from laboratory experiment and finite-difference

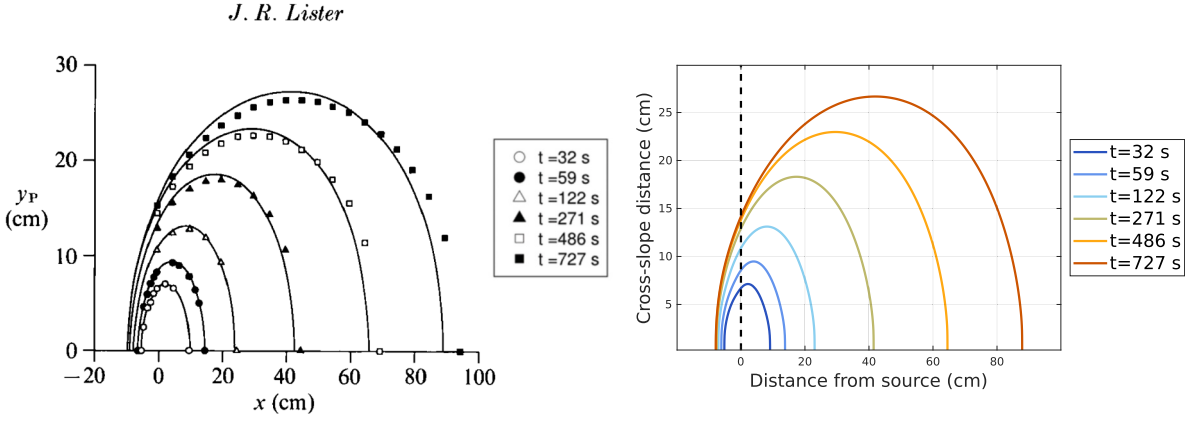

Fig. 2. Inclined viscous isothermal spreading. Representation at various times of the flow front. Left: results from Lister (Lister, 1992), where lines describe the evolution of laboratory experiment while symbols describe the predicted results obtained from numerical simulations. Right: results obtained by our code.

numerical simulation performed by (Lister, 1992) are reported; those are compared with results obtained by our numerical model (using the finest discretization grid) that are presented on the right. It is immediate to notice that, for all results represented, the up-slope extent rapidly reaches a steady state, whereas the flow continues to advance down-slope with time.

(Lister, 1992) determined a characteristic time t^* that separates two different behaviours of the spreading. Initially, for the so said "short time", fluid spreads radially from the source, as if it is on a horizontal plane. After that, for the so said "long time", the opposite occurs, and the flow is predominantly down-slope, with some cross-slope spreading. This behaviour is due to the pressure terms in the momentum equation (Eq. (27b)) that we rearrange as follows:

$$\int_B^{B+h} \nabla p(z)dz = \nabla\left(\frac{1}{2}\rho g h^2\right) + \rho g h \nabla B = \rho g h \nabla h + \rho g h \nabla B.$$

For the short-time behaviour, the term with the thickness gradient ∇h is bigger than the other one with the topography gradient ∇B, so the effect of the topography is almost negligible. Conversely, for the long-time dynamic, the term with ∇B becomes dominant, and then the flow mostly follows the topography. The short time dynamic is referred to as "density current", and the long time behaviour is named "avalanche" (de' Michieli Vitturi et al., 2019).

According to the definition given by (Lister, 1992), the characteristic time depends on several physical parameters proper of the test:

$$t^* = \left[\frac{(cot\alpha)^5}{R}\left(\frac{3\nu}{g sin\alpha}\right)^3\right]^{1/4}, \tag{29}$$

and in our case its value is ≈ 38 s. Fig. 3 presents the evolution of the fluid extent along the three directions, namely down-slope, cross-slope and up-slope, of our simulation and confirms that our dynamics are almost symmetric before the characteristic time. We also compare our results with the theoretical functions derived in (Lister, 1992) for the "long time" dynamics, confirming a reasonable asymptotic agreement, see (Biagioli, 2021).

We have extrapolated the down-slope and cross-slope extents of the laboratory test made in (Lister, 1992) from the original graph (depicted in Fig. 2) to compare our results with them as a convergence study. Table 2 reports the data collected, denoted as L_d and y_P, respectively and Fig. 4 shows a good agreement of the numerical simulation with the laboratory data.

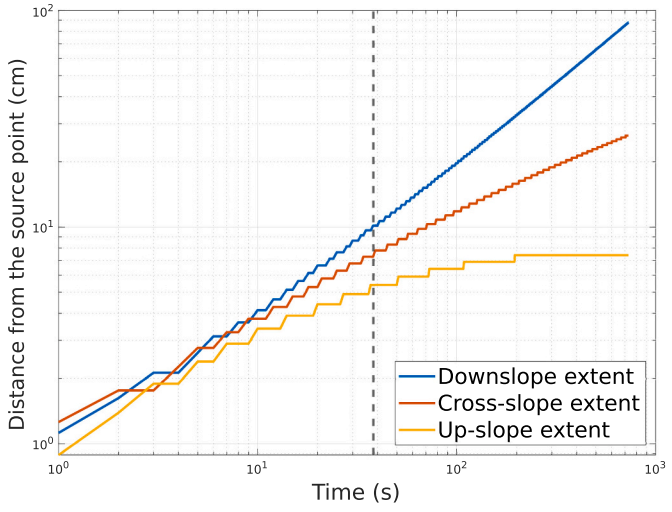

Fig. 3. Inclined viscous isothermal spreading. Time evolution of the down-slope, cross-slope and up-slope extents. The dashed line refers to the characteristic time t^*, defined in Eq. (29). The results illustrated were computed with the high-resolution spatial discretization.

Table 2
Inclined viscous isothermal spreading. Down-slope L_d and cross-slope y_P extents extrapolated from the laboratory experiment results (Fig. 2 on the left) that come from (Lister, 1992).

time (s)	32	59	122	271	486	727
L_d (cm)	9.5	14.5	23.5	42.5	65.5	88.5
y_P (cm)	7.0	9.4	13.0	18.4	23.3	27.2

The segmented style of Figure 3 and Figure 4 is due to the dimension of the computational cells. This is more evident in Fig. 4, which compares the results of the high-resolution and low-resolution simulations: the low-resolution simulation presents "steps" that are two times wider than those obtained by the high-resolution simulation. This happens because the cell size used for the low-resolution simulation is twice the size used for the high-resolution simulation. Fig. 3 presents the same stepping behaviour, which is not uniformly displayed because of the use of the logarithmic scales.

All the simulations presented for this benchmark are obtained under the assumption of a parabolic velocity profile ($\beta_u = 1.2$); however, using a constant velocity profile ($\beta_u = 1.0$) produces similar results anyway. This behaviour is unsurprising because, although the fluid has low viscosity, it moves very slowly, and the dynamics are driven by the gravity force instead of inertia. The fact that the motion is not led by inertia is the reason why this case is not much sensitive to the velocity profile assumption. For more details, see (Biagioli, 2021).

The execution time for 730 s of the high-resolution simulation computed by an Intel® Core™i7-6500U CPU, 2.50 GHz × 4 processor is about 5700 s (approximately 1 h and a half).

We point out to the reader that even (Dietterich et al., 2017; Zago et al., 2019) present results for the current benchmark. The former paper shows a comparison of performances of different models (such as VolcFLow (Kelfoun and Vargas, 2016), MOLASSES (Connor et al., 2012; Kubanek et al., 2015), and a solver written with OpenFOAM); the only observation we might add is that our model presents one of the best performances from the comparison of Fig. 4 with Figure 2.a presented in (Dietterich et al., 2017). Instead, (Zago et al., 2019) introduces a preliminary validation of a 3D model named GPUSPH. A direct comparison between their model and ours is hard to achieve because of their different intrinsic nature.

3.2. Axisymmetric cooling and spreading

This benchmark is related to a warm viscous fluid spreading onto a flat plane and cooling down due to heat exchanges with the environment. Such a test is an intermediate proposal between the spreading-only benchmarks and the most complex lava flow case that follows. Viscosity is assumed Newtonian and temperature-independent, so there is no relation between rheology and thermal structure.

This test is born from an analogue experiment reported in (Garel et al., 2012) (originally denoted as C14) where a hot silicone oil (Rhodorsil® 47 V 5000 or 47 V 12500, dyed red) is injected at a constant supply rate $2.2 \cdot 10^{-8}\,m^3\,s^{-1}$ onto a horizontal plane of polystyrene from a point source of 2–4 mm of radius. Table S1, Supplementary Material §S.2, reports the values of the physical parameters involved in the experiment. (Cordonnier et al., 2015) reports most parameters, while all the others are available only on the original paper (Garel et al., 2012). However, there is a difference in the density value indicated in the two papers, and we adopted the value of 954 $kg\,m^{-3}$ reported in the original work by (Garel et al., 2012) (instead of 886 $kg\,m^{-3}$ referred in (Cordonnier et al., 2015)).

The square $[-12\,cm,\ 12\,cm] \times [-12\,cm,\ 12\,cm]$ determines the computational domain that we discretize with two different grid resolutions, a coarse one with $\Delta x = 2 \cdot 10^{-3}\,m$ and a finer one with $\Delta x = 10^{-3}\,m$, respectively low and high resolution. The circular vent is located in the domain centre and is approximated by discretization via grid squares. The mass flux through these source cells is not equal in

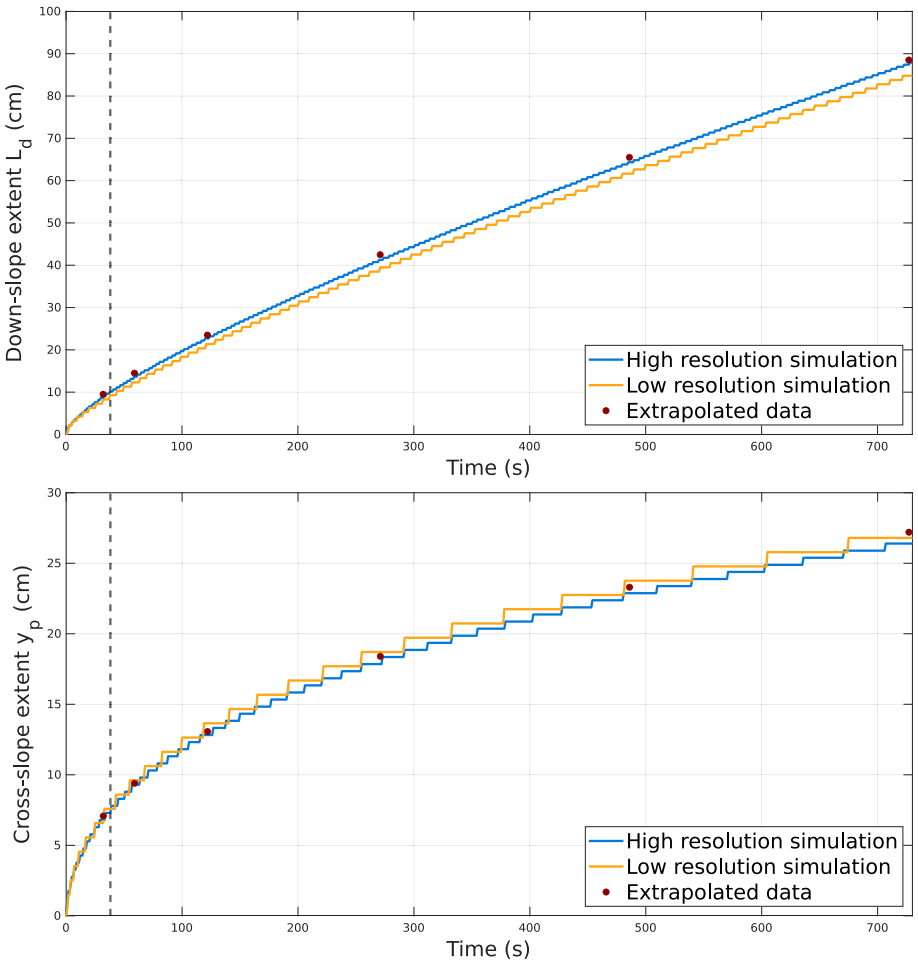

Fig. 4. Inclined viscous isothermal spreading. Time evolution of the down-slope extent $L_d(t)$ (top) and the cross-slope extent $y_P(t)$ (bottom). The extrapolated data refer to Table 2. The dashed line refers to the characteristic time t^*, defined in Eq. (29).

every cell but is proportional to the fraction of the cell that belongs to the vent. From the modelling point of view, we adopt the parabolic velocity profile, with $\beta_u = 1.2$, and the piecewise linear temperature profile, with β_T defined in Eq. (17). The thermal boundary layers parameters are $n = 4$ for the oil and $M = 12$ for the polystyrene surface, whereas the fraction of the exposed inner core in Eq. (21) is $f = 1$ because the fluid is fully melted. Since the viscosity does not depend on temperature, the rheological parameter of Eq. (9) is $b = 0$.

The experiment dynamics are symmetric with a "radial" flow advance. Despite using a cartesian grid, the simulation manages to reproduce the radial propagation thanks to the choice of the spatial discretization scheme and the source discretization. Fig. 5 depicts the evolution of the fluid thickness taken at a vertical slice passing through the vent. Initially, the fluid has uni-axial inflation developing only one central bulge. Later, the lateral spreading becomes dominant, lateral bulges develop too, and the central bulge above the feeding pipe quite reaches a steady state. We also performed a convergence study that shows the good agreement of our numerical results with the analytical solution determined in (Huppert, 1982), see (Biagioli, E., 2021). Notice that in every plot reported, we only show values of the thickness h greater than 10^{-4} m, which is reasonable considering the fluid thickness represented in Fig. 5.

Figure 6 shows an analysis of the temperature evolution: our results are compared with experimental and theoretical data of the original paper (Garel et al., 2012). Temperature and radial distance from the source are normalized, so $x = 1$ corresponds to the fluid front. This comparison proves that our results agree better with the experimental outcomes than with the theoretical ones. The Supplementary Material §S.2 presents another figure that compares the temperature computed with our simulation to the original data collected from the laboratory test, Fig. S2, and that shows a good agreement of our numerical results with the experimental results.

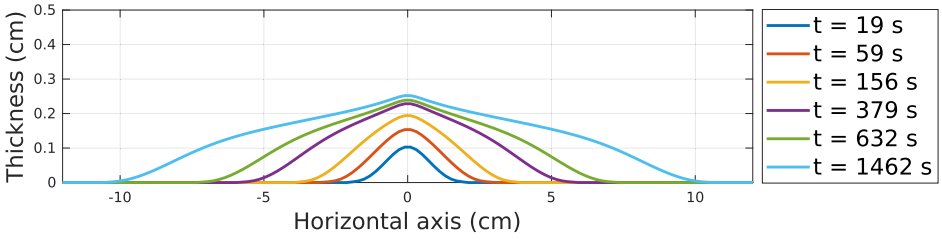

Fig. 5. Axisymmetric cooling and spreading. The thickness of the simulated fluid at different times.

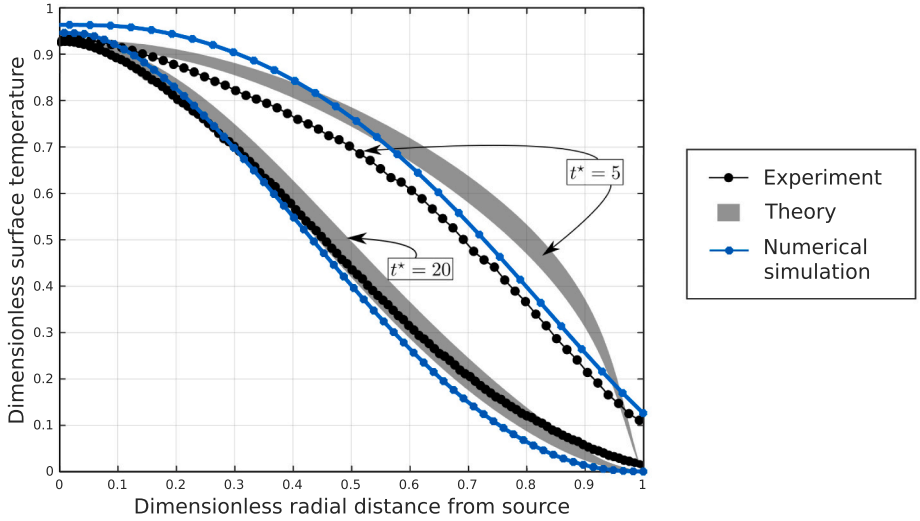

Fig. 6. Axisymmetric cooling and spreading. Comparison of experimental, theoretical and simulated normalized surface temperatures, defined as $(T - T_{env})/(T_{vent} - T_{env})$, over the normalized radial distance. $t^* = 5$ corresponds to $t = 156$s and $t^* = 20$ to $t = 620$s. In the original work (Garel et al., 2012), t^* is defined as $t^* = t/\tau$ where $\tau = 0.715^{4/3}[3\mu R/(\rho g)]^{1/2}/\kappa$.

The execution time for 632 s of the high-resolution simulation computed by an Intel® Core™ i7-6500U CPU, 2.50 GHz × 4 processor is about 1400 s (approximately 3 h and 50 min).

The works (Biagioli, 2021; Dietterich et al., 2017; Zago et al., 2019) present results concerning the current benchmark. As stated previously for the former test, the first paper shows the comparison of performances of different models, whereas the second article introduces a preliminary validation of a 3D model named GPUSPH. The third reference presents this simulation performed by means of an OpenFOAM 3D solver. The reader might compare Fig. 6 with Figure 10 presented in (Zago et al., 2019) and appreciate that, despite an overestimation of the values, our simulation results are closer to the experiment data, especially on the external part of the fluid at the time $t = 5$.

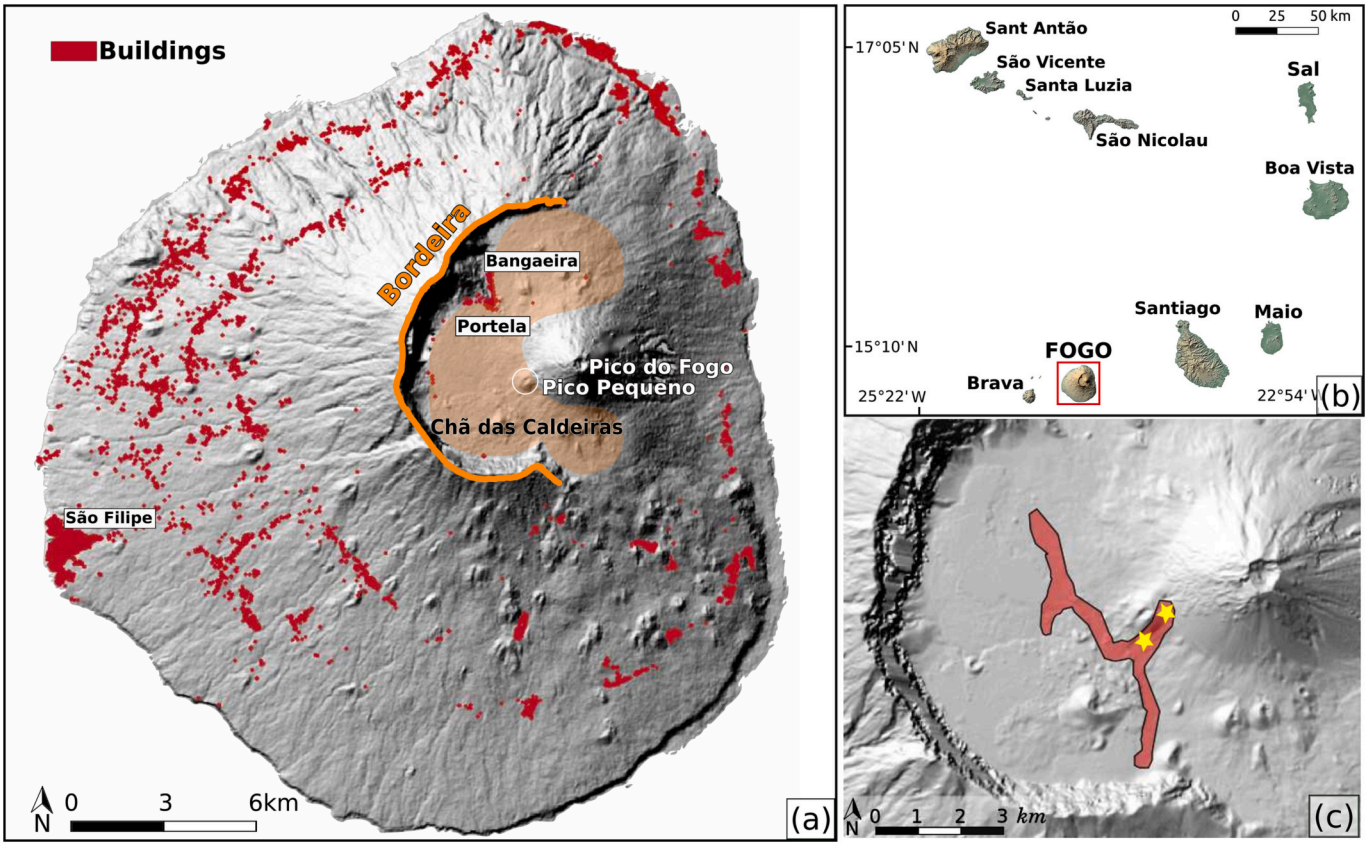

Fig. 7. Natural case. (a) Map of Fogo Island. (b) Archipelago of Cape Verde, of which Fogo is a part. (c) Lava emplacement of the real event after one day of the eruption, on 24 November 2014, is represented by an outline extracted from (Cappello et al., 2016) defined based on field mapping and satellite images. The stars represent the extrema of the fissural vent.

3.3. Natural case: the Pico do Fogo 2014–2015 eruption

In general, models for lava flows work well when there are high slopes, namely where the gravitational term dominates in the transport. On flatter, shallow slope topographies, the accuracy of the models in treating viscous and inertial terms becomes more important. For this test, we applied our model to the eruption of the Fogo volcano, Cape Verde, West Africa, which started on 23 November 2014 and ended on 8 February 2015. We chose this event because the eruption developed on an almost flat topography, a condition where the rheology significantly impacts the lava emplacement, making this event ideal for testing the model's accuracy. Also, this event is well-documented, so the input data and the lava emplacement were easy to find. In this test, we use the real topography before the eruption and characteristic parameters of the lava flow event, i.e. the vent location, effusion rate, and effusive temperature, to simulate the eruption's first day.

Cape Verde Archipelago is located west of the Western Atlantic coast of Africa and has volcanic origins (Day et al., 1999). Fogo Island rises between Brava and Santiago islands and is the fourth largest island of the archipelago and the highest at 2829 m above the sea level of Pico do Fogo, see Fig. 7 (b). An active volcano stands in the island's centre, presents a 9 km wide caldera, Chã das Caldeiras ("Plain of the Calderas"), and has its summit at Pico do Fogo. An enormous crater rim, called Bordeira and up to 1 km high, encircles the caldera on its western side, Fig. 7 (a). Fogo volcano is the youngest and most active volcano of the archipelago (Courtney and White, 1986; Dionis et al., 2015).

Topography and vent location have a major impact on real events simulation, so all numerical codes, including those that do not consider rheology and temperature, have to use topographic data. The more accurate the topography and the vent position are, the more reliable the results will be. In our simulations, we used a DEM (Digital Elevation Model) generated from SAR satellite images with data acquired in 2011–2013 and with a horizontal resolution of 12 m (the DEM of Fogo is a TanDEM-X WorldDEM[2] data (Rizzoli et al., 2017) provided by the German Aerospace Center (DLR) through data proposal DEM_GEOL_1522, PI Nicole Richter). The eruptive source was a fissure that opened on the southwest flank of Pico do Fogo. Richter et al. (Richter et al., 2016) (who estimated the lava flow hazard at Fogo by using the probabilistic code DOWNFLOW (Favalli et al., 2005; Tarquini and Favalli, 2011)) used a single vent that corresponded to the highest end of the fissure (DMS coordinates: 14° 56′ 40.56″ N - 24° 21′ 12.28″ W; UTM coordinates: East 784,689.69 - North 1,653,895.03, zone 26P). Instead, the work (Cappello et al., 2016) observed that the other end of the fissure, the lowest, was the main source of lava. Having this discordant information, we decided to consider both vents, using the following position for the lowest one, DMS coordinates 14° 56′ 27.15″ N - 24° 21′ 22.96″ W; UTM coordinates East 784,375.00 - North 1,653,479.0, zone 26P. The vents' position is reported in Fig. 7 (c).

(Cappello et al., 2016) used HOTSAT, a satellite thermal monitoring system, to retrieve details such as the lava thermal flux and the effusion rate. For the first day of eruption (Fig. 7 (c) shows the corresponding lava emplacement that is extracted from (Cappello et al., 2016) and defined based on field mapping and satellite images), they recorded a mean effusion rate of 10.5 $m^3 s^{-1}$, with peaks between 24 and 27 $m^3 s^{-1}$. We adopt their mean value as a constant effusion rate since there is no information about the time variations and consider 20 m of radius for the vents. They estimated the extrusion temperature to be 1265°C (1538 K), and we use that as T_{vent}. Moreover, we adopt their suggested values for density ρ (2600 kg m^{-3}) and specific heat capacity c_p (1150 J kg^{-1} K^{-1}) that are typical values of basaltic magma, as it is for Fogo.

The Bingham plastic rheology model with temperature-dependent viscosity (Eqs. (8–9)) is adopted, assuming as reference values for temperature T_{ref} and for dynamic viscosity μ_{ref} those at the vent, consequently $T_{ref} = T_{vent} = 1538$ K. The values of dynamic viscosity, rheological parameter b, and yield stress vary in the context of the sensitivity analysis among reasonable values for basaltic magma, as described in the following. Values for lava thermal conductivity, emissivity, exposed area inner fraction, atmospheric heat transfer, and environmental temperature are those suggested in (Costa and Macedonio, 2005) for Etna effusive eruptions, as Etna and Fogo magmas are both basaltic. Soil thermal conductivity is taken from (Darkwa et al., 2013). Table S2, in the Supporting Material, reports all the adopted physical parameters and the temperature profile characteristic values (n, M and T_{soil}).

It is worth mentioning that this test is not meant to reproduce exactly the actual natural event as close as possible but instead to analyze the impact that the rheological parameters have on lava flow emplacement. First, we present the effect of different grid resolutions on the results (obtained with a set of parameters chosen from the sensitivity analysis). As the spatial discretization grid with 40 m × 40 m cells stands out as a good trade-off between the solution accuracy and the computational time, this resolution has been used for all the other investigations. The sensitivity analysis then follows to enquire about the role of the rheological parameters on the lava flow emplacement. After such analysis, we finally investigate the impact of different vent positions on the solution. We specify that, in all figures, we plotted results by applying a 1 cm threshold to the flow thickness. A choice of a thinner thickness threshold impacts (however negligibly) only those simulations with small yield stresses (because the higher the yield stress, the thicker the lava front, as shown in the following).

3.3.1. Grid resolution test

The sensitivity of numerical outcomes to the grid resolution is tested by comparing simulations obtained with three different cell sizes (see Fig. 8): coarse 80 m × 80 m cells, medium 40 m × 40 m cells, and fine 20 m × 20 m cells. The rheological parameter values adopted (that come from the sensitivity study upcoming in the following section) are $\mu_{ref} = 100$ Pa s, $b = 10^{-3}$ K^{-1}, and $\tau_0 = 750$ Pa. The result obtained by the coarse mesh is far from the one computed with the fine mesh. On the other hand, the runout computed by the medium mesh is comparable to that over the fine mesh. We conclude that simulations produced using a mesh 40 m × 40 m are reliable. Table 3 shows the execution time of the three simulations computed by an Intel® Core™ i7-6500U CPU, 2.50 GHz × 4 processor. The short execution times allow the use of our model also for hazard quantification and for the production of probabilistic maps owing to the simulation's short duration.

3.3.2. Rheological parameters sensitivity study

In this sensitivity analysis, we vary the values of three rheological parameters, namely, the dynamic viscosity at the vent, μ_{ref}, the yield stress, τ_0, and the rheological parameter b, within reasonable ranges as described in the following.

Based on previous studies (Chevrel et al., 2020; Harris et al., 2016; Kolzenburg et al., 2018; Rhéty et al., 2017), the dynamic viscosity of basaltic magma upon eruption is estimated to be in the range of 10^2–10^4 Pa s. Therefore, we use three values for μ_{ref} equal to 10^2, 10^3, and 10^4 Pa s. (Bernabeu et al., 2016) assessed the basaltic lava yield stress τ_0 in the range 10^2–10^4 Pa, and we select three values 10^2, 10^3, and 10^4 Pa. Additionally, to simulate the Newtonian behaviour, we set $\tau_0 = 0$ Pa. The viscosity exponent b has been adopted as $2{\cdot}10^{-2}$ K^{-1} (Costa and Macedonio, 2005) for a simulation of Etna volcano, and a similar value, $1.6{\cdot}10^{-2}$ K^{-1} has been used by (Bernabeu et al., 2016) (both simulations are relative to basaltic lava). We opt to test the values

[2] The TSX/TanDEM-X mission is for the creation of a global, consistent, and high-resolution Digital Elevation Model (DEM) obtained by exploiting the interferometric capabilities of the two twin SAR satellites TerraSAR-X and TanDEM-X, which fly in a close orbit formation. The work for the creation of this global DEM lasted from December 2010 to September 2016.

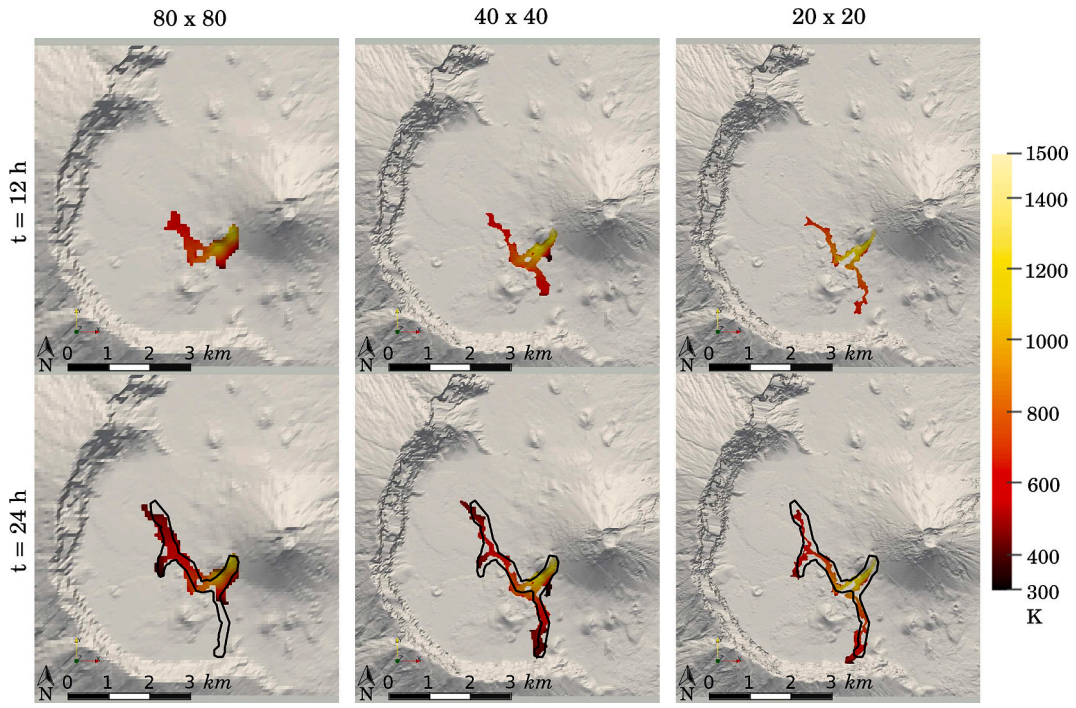

Fig. 8. Natural case. Sensitivity to the computational grid size. Left: grid size 80 m × 80 m, grid dimensions 100 × 100 cells. Center: grid size 40 m × 40 m, grid dimensions 200 × 200 cells. Right: grid size 20 m × 20 m, grid dimensions 400 × 400 cells. Simulations of 24 h of eruptions computed with reference viscosity $\mu_{ref} = 100$ Pa s, rheological parameter $b = 10^{-3}\,\mathrm{K}^{-1}$, and yield stress $\tau_0 = 750$ Pa. The black line represents the real lava emplacement after one day of the eruption. See Fig. S3 in Supplementary Material §S.4 for a more detailed chronology.

Table 3
Natural case. Elapsed time for the execution of simulations by different grid sizes; simulations of 24 h of eruptions computed using reference viscosity $\mu_{ref} = 100$ Pa s, rheological parameter $b = 10^{-3}\,\mathrm{K}^{-1}$, and yield stress $\tau_0 = 750$ Pa. Processor specifications: Intel® Core™ i7-6500U CPU, 2.50 GHz × 4.

Cell dimensions	80 m × 80 m	40 m × 40 m	20 m × 20 m
Time	100 s	539 s	2606 s
Total number of cells	10^4	$4{\cdot}10^4$	$16{\cdot}10^4$

of $b = 10^{-2}\,\mathrm{K}^{-1}$, $10^{-3}\,\mathrm{K}^{-1}$ and $b = 0\,\mathrm{K}^{-1}$ (indicating viscosity independent from temperature).

Figure 9 presents the thickness and temperature of the lava flow after 24 h of the eruption, considering $\mu_{ref} = 10^2$ Pa s and varying yield stress τ_0 and rheological parameter b. Similar results for $\mu_{ref} = 10^3$ and 10^4 Pa s can be found in Figs. S4 and S5 in Supplementary Material §S.5. From the comparison of results, we make two observations. First, increasing the yield stress leads to narrower and taller lava flow emplacements. Secondly, we analyze the role of the parameter b. From the analytical expression of the temperature-dependent viscosity, Eq. (9), we get that for $b = 10^{-2}\,\mathrm{K}^{-1}$ there is the strongest coupling between temperature and velocity because temperature has the greatest influence on viscosity. In this case, regardless of the other parameters, the lava emplacement is not significantly affected by the topography and remains confined in an area close to the vents. An exception to this is observed when $\tau_0 = 10^4$ Pa, where it is evident that lava follows the topography although the flow propagation is still limited. Simulations with $b = 0$ K^{-1} (constant viscosity and decoupling between temperature and momentum equations) exhibit very different results, showing a high sensitivity to the details of the topography. The case with $b = 10^{-3}\,\mathrm{K}^{-1}$ presents results that are more similar to the decoupled case ($b = 0$ K^{-1}) but still reflect the dependence of viscosity on temperature.

For all the three reference viscosity considered, the largest emplacement area of each figure occurs in the decoupled Newtonian case ($b = 0$ K^{-1}, $\tau_0 = 0$ Pa). This is because lower viscosity results in a larger surface area being inundated. Specifically, Fig. 9 presents the largest final emplacement among all simulations.

3.3.3. Real event parameters estimation

Our further attempt is to determine ranges for the values of b, μ_{ref}, and τ_0 that produce simulations compatible with the real event and to study their effects on the runout. By comparing the results of the previous sensitivity analysis with the emplacement of the real event (see Fig. 9 and Figs. S4 and S5 in Supplementary Material §S.5), we notice that simulations obtained with $b = 10^{-3}\,\mathrm{K}^{-1}$, $\tau_0 = 10^2,\ 10^3$ Pa and $\mu_{ref} = 10^2,\ 10^3$ Pa s present more similarities with the real case, prompting us to perform further investigations. To provide a more accurate description of the solution dependence on such parameters, we fix the parameter b and let τ_0 and μ_{ref} assume some values in the range $10^2 - 10^3$.

Figure 10 depicts the thickness (in the logarithmic scale) of the simulations performed. Supplementary Material §S.6 presents more figures related to this analysis, depicting temperature and viscosity. Comparing the results shown in Figure 10 with the real lava emplacement after one day of the eruption, we observe that the simulations obtained with $\mu_{ref} = 100$ Pa s and $\tau_0 = 500, 750$ Pa best reproduce the real event. Since more than one simulation shows a good agreement with the observations, we select a single set of parameters to continue with further analysis: namely $\mu_{ref} = 100$ Pa s and $\tau_0 = 750$ Pa.

To examine the temporal evolution of the first 24 h of the eruption with the chosen parameters ($b = 10^{-3}\,\mathrm{K}^{-1}$, $\mu_{ref} = 100$ Pa s and $\tau_0 = 750$ Pa), Fig. S9 in the Supplementary Material §S.7 is presented.

3.3.4. Study on the vent position

In the simulations presented so far, we have assumed that two vents feed the flow. In order to analyze the effect of this assumption, Fig. 11 compares the results of simulations obtained considering both vents

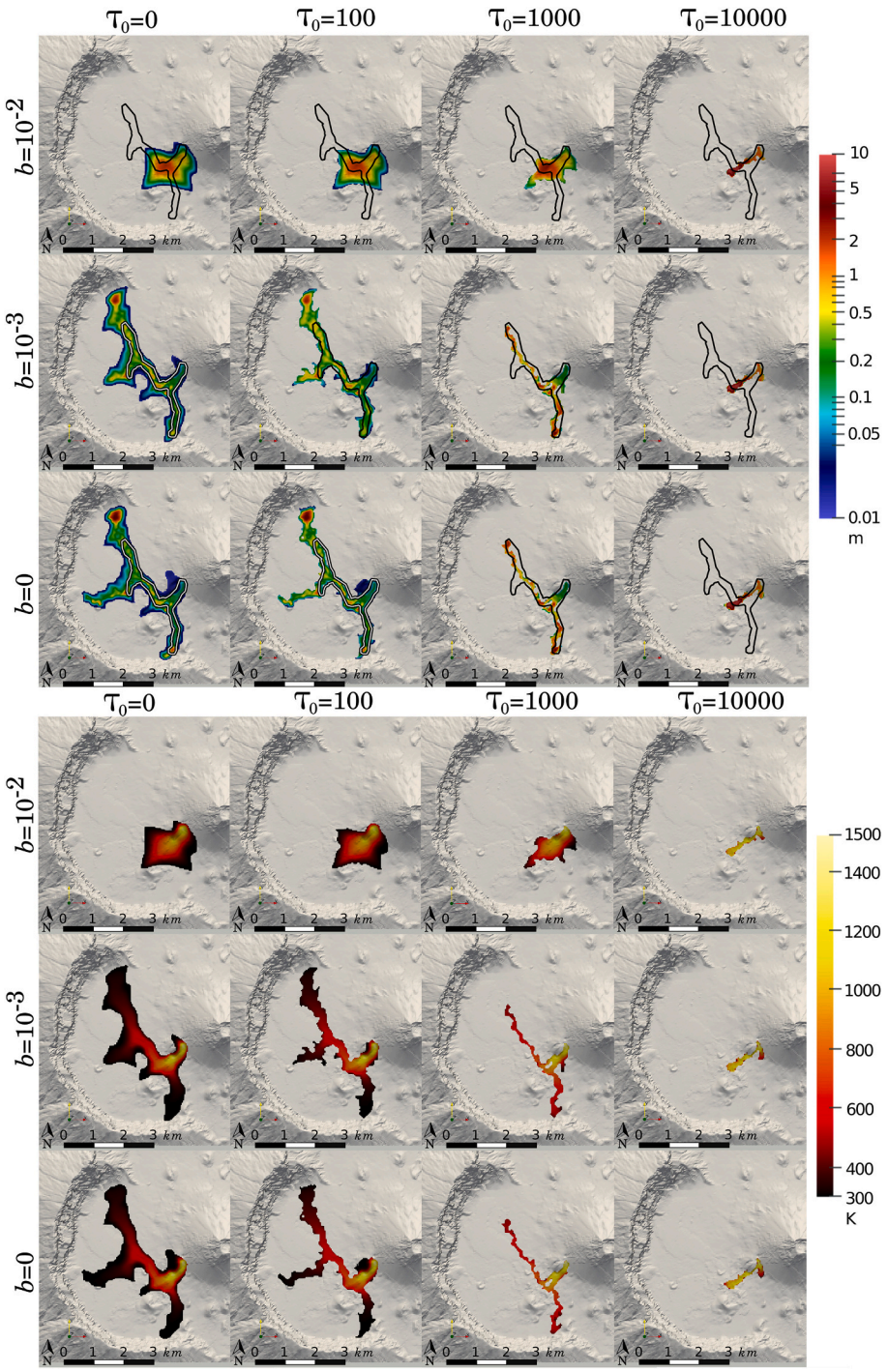

Fig. 9. Natural case. Rheological parameters sensitivity study. Simulations after 24 h of eruptions computed with a grid size of 40 m, considering $\mu_{ref} = 10^2$ Pas, varying the yield stress τ_0 (Pa) and the parameter b (K^{-1}). The black line represents the real lava emplacement after one day of the eruption. Top: thickness (in logarithmic scale). Bottom: temperature.

versus only one of them. While the final lava flow emplacements do not differ significantly, we can observe that in cases where only one vent is adopted, the final front propagates more towards either north or south. This highlights the importance of choosing the vent location accurately and considering any changes that may occur during an eruption in order to achieve amore accurate description of lava flow emplacement.

Finally, we point out to the reader that the paper (Cappello et al., 2016) presents results of simulations concerning the Pico do Fogo eruption. Fig. 5 (top picture) reported in (Cappello et al., 2016) represents the simulation of the lava flow thickness after the first day of activity. This result may be compared with our Fig. 10 (picture with $\mu_{ref} = 100$ Pas and $\tau_0 = 750$ Pa) and Fig. 11 (picture on the right). Both simulations, ours and the one in (Cappello et al., 2016), overestimate the real propagation extent at the north lobe. Our simulation propagates more towards the south and the west lobes, still remaining inside the contour of the real event, with respect to the simulation in (Cappello et al., 2016) that, instead, underestimates these extensions.

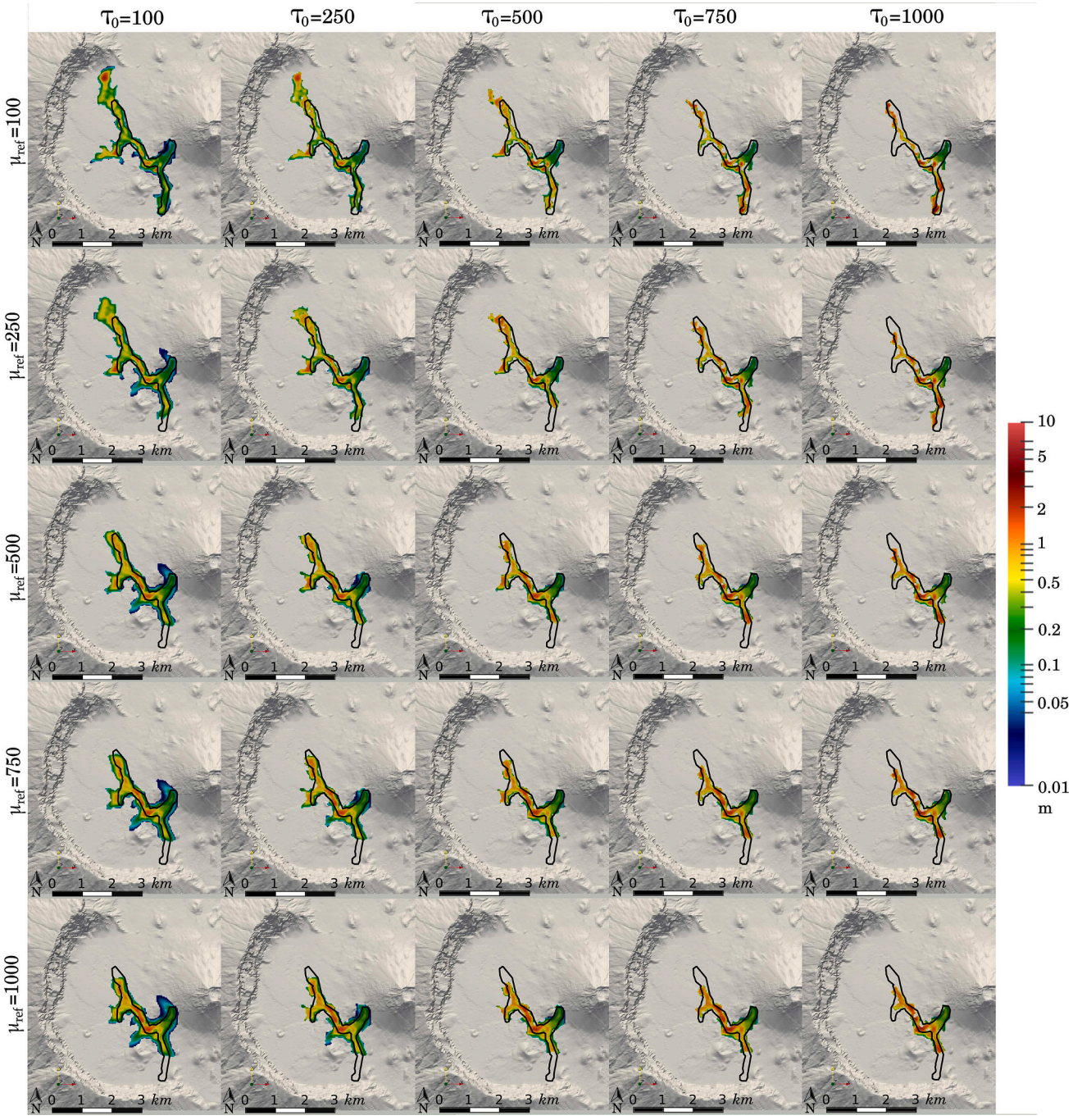

Fig. 10. Natural case. Real event parameters estimation: thickness (in logarithmic scale). Simulations after 24 h of eruptions computed with a grid size of 40 m, fixing $b = 10^{-3}\,\mathrm{K}^{-1}$ and varying both the yield stress τ_0 and the reference viscosity μ_{ref} in the range $100 - 1000$. The black line represents the real lava emplacement after one day of the eruption.

4. Conclusions

This paper presents a new physical-mathematical model for lava flow emplacement and its validation with the numerical simulation of two well-established benchmarks and a real-case scenario.

We modelled lava as a hot and viscous fluid in a laminar regime that cools because of radiative and convective heat loss from the surface to the environment and through conduction with the soil. Following a variant of the depth-averaged (or shallow-water) approach, we derive a system of hyperbolic partial differential equations that we solve by a finite-volume method. Unlike the classical shallow water equations, our 2.5D model accounts for velocity varying with the flow depth and assumes a parabolic profile to match the no-slip condition at the bottom in a laminar regime. Moreover, the viscosity may depend on temperature, and the rheology model can be Newtonian or Bingham plastic. Because of the conduction with the soil, temperature develops a thermal boundary layer that is accounted for by the 2.5D model assuming a piecewise-linear profile. Finally, a transport equation models the temperature evolution by considering the thermal heat exchanges and the viscous heating. The flux terms of the momentum and temperature equations present corrector factors due to the assumptions on the vertical profiles.

The numerical scheme used here is a central-upwind Finite Volume Method, relatively simple to implement, that presents a low numerical

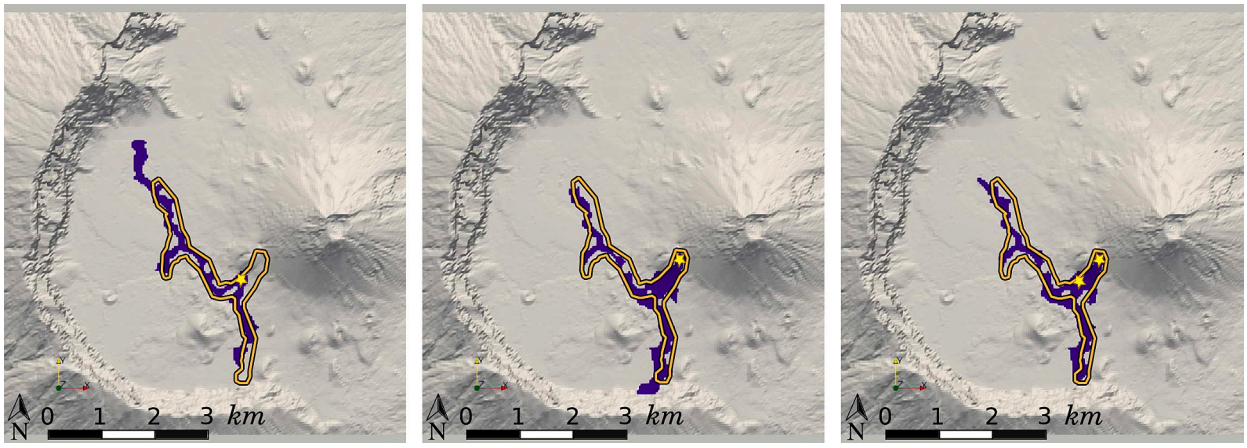

Fig. 11. Natural case. Sensitivity to the vent position. We call V1 and V2 the two vents we employed in our simulations: V1 (DMS coordinates: 14°56′40.56″ N - 24°21′12.28″ W; UTM coordinates: East 784,689.69 - North 1,653,895.03, zone 26 N), and V2 (DMS coordinates: 14°56′27.15″ N - 24°21′22.96″ W; UTM coordinates: East 784,375.00 - North 1,653,479.0, zone 26 N). Left: we used V1, the highest vent. Center: the lowest vent V2 was adopted. Right: both vents were used. Simulations after 24 h of eruptions computed with a grid size of 40 m, reference viscosity $\mu_{ref} = 100$ Pa s, rheological parameter $b = 10^{-3}$ K^{-1}, and yield stress $\tau_0 = 750$ Pa. The line represents the real lava emplacement after one day of the eruption.

diffusion (being a high-order scheme) and satisfies both the positivity-preserving and well-balancing properties (guaranteeing that the numerical scheme correctly describes steady-state solutions). The temporal discretization explicitly treats the advective terms and implicitly treats the viscous term in the momentum equation and the heat transfer terms in the temperature equation.

We made simulations to validate the model with well-established benchmarks for lava flow models and the real-case scenario of the 2014–2015 Pico do Fogo, Cape Verde, eruption. By comparing simulation results with the two laboratory experiments, the model has proven to be able to properly reproduce the spreading of an isothermal viscous fluid over an inclined plane and the cooling due to heat exchanges with the environment.

As regards the real case scenario, we chose the 2014–2015 Pico do Fogo, Cape Verde, eruption because it developed on an almost flat topography. The rheology significantly impacts the lava emplacement in this condition, making this event ideal to test the model's accuracy. In general, lava flow models work well in the presence of high slopes for whom the gravitational term dominates in the momentum transport. On flatter, shallow slope topographies, the accuracy of the models in treating viscous and inertial terms becomes more important. For this reason, the stochastic models, for example, work well on topographies with high slopes and show problems in other cases.

The main results of our work on this real case test are summarised in the following. We conducted a sensitivity analysis of the temperature-dependent Bingham rheological model parameters to test their impact on the final lava flow emplacement. The cases with the strongest coupling between temperature and momentum equations ($b = 10^{-2}$ K^{-1} in Eq. (9)) correspond to a greater temperature influence on viscosity. In such cases, the lava emplacement is less affected by the topography and remains close to the vents, almost independent of the other parameters. The case with the highest yield stress considered here, i.e. $\tau_0 = 10^4$ Pa in Eq. (8), represents an exception as lava follows the topography, despite the flow propagation being limited, owing to increasing the yield stress, which results in a narrower and thicker lava flow emplacement. The simulations where the temperature and momentum equations are decoupled ($b = 0$ K^{-1}), and the viscosity is constant, produce the largest inundated areas. Indeed, the viscosity remains equal to the value at the vent, at the emission temperature, thus, viscosity stays lower compared to the temperature-dependent cases. The cases with a weak decoupling ($b = 10^{-3}$ K^{-1}) show results different from those obtained with the strongest coupling, being more similar to the decoupled case. Lastly, simulations that use the highest viscosity at the emission ($\mu_{ref} = 10^4$ Pa s in Eq. (9)) underestimate the lava flow extent greatly with respect to the real situation.

We also investigated the impact of vent position and grid resolution on lava emplacement. Despite the lava flow being erupted from a fissure system, here we use circular vents, and we prove that placing two vents located at both ends of the fissure produces results that are significantly closer to the real lava emplacement than those obtained by considering only one of the two vents. Finally, the sensitivity analysis to the grid resolution, intimately linked to the topography accuracy, is tested by using three cell sizes: coarse with 80 m × 80 m cells, medium with 40 m × 40 m cells, and fine with 20 m × 20 m cells. The coarse mesh produces a result far from the real lava flow emplacement, probably because of an imprecise topography description. Instead, the results obtained with the fine and medium meshes show a good fit with the real event and are computed in approximately 40 and 10 min, respectively.

The accuracy of the simulations is often given in terms of the flow extent by comparisons with laboratory data, analytic data, and real data. Besides performing this kind of analysis, we also showed the fluid thickness, viscosity, and temperature with this model (the velocity field is another variable that can be addressed by our model, but its analysis was out of the purposes of our work, so we did not show it). The knowledge of the temporal evolution of the spatial distribution of these variables allows for further investigations of the model's accuracy.

In summary, our model is capable of accurately reproducing both isothermal and non-isothermal laboratory tests and producing a good fit with the real lava flow of the Fogo eruption. The latter application of the model showed promising results regarding real event description and computational time required for the simulation. It is worth highlighting that the short execution times specified above allow using our model also for hazard quantification and generating probabilistic maps, as many simulations can be performed in a short time. This makes our lava flow model a tool well-suited for use in volcano observatories during real-time eruption crises.

4.1. Limits and future developments

It is important to highlight that the set of equations we derived is based on strong assumptions on the velocity and temperature profiles, and these assumptions carry with them some limitations. As already written, the assumption of a temperature-dependent viscosity for a fluid with a vertical temperature profile would lead to the development of a vertical profile also for viscosity (Hyman et al., 2022), and thus to a deviation to the parabolic velocity profile we used, which is based on a

constant viscosity profile. In the future, we plan to account for the effects of a non-constant viscosity profile on the velocity.

Future advances in our work also include improving the description of the vertical velocity profiles by considering a dynamic evolution for the profiles, allowing them to vary as a function of the local flow regime. For example, different velocity profiles can be designed as a function of the local Reynolds number, distinguishing between laminar and turbulent regions of the flow, or by introducing a plug profile, which can develop with a Bingham rheology (Tallarico and Dragoni, 2000). The thermal boundary layer thickness discussed above could be related to the velocity boundary layer thickness, with the ratio of the two thicknesses governed by the Prandtl number (the ratio of momentum to thermal diffusivity). However, these modifications require not only a rewriting of the set of equations, since the depth-averaging of non-constant profiles gives rise to new shape factors in some of the terms of the governing equations, but also further studies on the properties of the numerical schemes (well-balancing and positivity-preserving), which are not obvious when one modifies the model.

Under the hypothesis of negligible vertical velocity and hydrostatic pressure distribution, the shallow water models need further improvements to entirely capture fast dynamics that develop over terrain with high gradients. Natural processes that present those features are, for example, avalanches, landslides, and debris flow, but even lava flows may develop over steep terrain and flow fast. (Hergarten and Robl, 2015) proposed a modified shallow water model that introduces a correction factor for the friction term to better capture dynamics over a steep slope. (Xia and Liang, 2018) proposed another modified model that considers both the effects of the vertical acceleration and the consequences of curvature due to a complex terrain morphology, introducing inside the momentum equation correction factors for the pressure and friction terms. (Bachini and Putti, 2020) developed a geometrically intrinsic shallow water model defined on a local reference frame anchored to the bottom surface. As a future development, we plan to modify our model by following one of the former approaches to make it more flexible and applicable to a broader spectrum of cases.

Lava reaches the solidus temperature during the cooling process, becomes solid, and does not flow anymore. As we are accounting for a vertical thermal profile developed through ground conduction, we can expect that the solidus temperature is first reached at the flow base, close to the ground. A possible future development consists of describing the solidification at the ground by modelling the incorporation of an appropriate lava layer in the topography, where the layer thickness depends on its temperature. Anyway, cooling arises from the surface too, sometimes resulting in a dominant effect; therefore, further work should be also devoted to find a way to incorporate crust formation in the model.

Finally, we remind that the process of crystallization (induced by lava cooling) has a high impact on flow dynamics because it leads to a viscosity increase and possible flow stopping. This phenomenon can be explicitly treated by including an equation describing the transport of an additional phase, representing crystals, with a related source term modelling crystallization rate as a function of flow temperature and magma composition. Our future plan is to include this process in our model together with a rheological model capable of considering both temperature and crystal content by modifying the viscosity term.

Funding

The research leading to these results has received funding from UKRI FLF project 4DVOLC (MR/V023985/1).

Declaration of Competing Interest

The authors declare that they have no known competing financial interests or personal relationships that could have appeared to influence the work reported in this paper.

Data availability

The data used are directly available in the manuscript and supplementary material. The code is available at the link shared in the manuscript.

Acknowledgements

The authors acknowledge Prof. Einat Lev, Lamont-Doherty Earth Observatory at Columbia University, New York, for the precious collaboration and helpful discussions. The authors thank the reviewers whose observations contributed to improving the work's presentation.

TanDEM-X WorldDEM data were provided by the German Aerospace Center (DLR) through data proposal DEM_GEOL_1522, whose Principal Investigator is Nicole Richter, whom the authors thank for her gentleness and availability to collaborate.

Appendix A. Supplementary data

Supplementary data to this article can be found online at https://doi.org/10.1016/j.jvolgeores.2023.107935.

References

Avolio, M.V., Mirocle Crisci, G., Di Gregorio, S., Rongo, R., Spataro, W., Trunfio, G.A., Aug 2006. SCIARA γ2: an improved cellular automata model for lava flows and applications to the 2002 Etnean crisis. Comput. Geosci. 32 (7), 876–889. https://doi.org/10.1016/j.cageo.2005.10.026.

Bachini, E., Putti, M., 2020. Geometrically intrinsic modeling of shallow water flows. *ESAIM*. Math. Model. Num. Anal. 54 (6), 2125–2157. https://doi.org/10.1051/m2an/2020031.

Barca, D., Crisci, G.M., Di Gregorio, S., Nicoletta, F., 1994. Cellular automata for simulating lava flows: a method and examples of the Etnean eruptions. Transport Theory Statist. Phys. 23, 195–232. https://doi.org/10.1080/00411459408203862.

Barca, D., Crisci, G.M., Rongo, R., Di Gregorio, S., Spataro, W., 2004. Application of the Cellular Automata Model SCIARA to the 2001 Mount Etna Crisis. American Geophysical Union, Geophysical Monograph Series, pp. 343–356. https://doi.org/10.1029/143GM21.

Batchelor, G.K., 2000. Equations Governing the motion of a fluid. In: Cambridge Mathematical Library. Cambridge University Press, pp. 131–173. https://doi.org/10.1017/CBO9780511800955.005.

Bernabeu, N., Saramito, P., Smutek, C., 2016. Modelling lava flow advance using a shallow–depth approximation for three–dimensional cooling of viscoplastic flows. Geol. Soc. Lond. Spec. Publ. 426 (1), 409–423. https://doi.org/10.1144/SP426.27.

Biagioli, E., de' Michieli Vitturi, M. IMEX_LavaFlow. doi: https://doi.org/10.5281/zenodo.2553101. URL https://github.com/BiElisa/IMEX_LavaFlow.

Biagioli, E., de' Michieli Vitturi, M., Di Benedetto, F., 2021. Modified shallow water model for viscous fluids and positivity preserving numerical approximation. Appl. Math. Model. 94, 482–505. https://doi.org/10.1016/j.apm.2020.12.036.

Biagioli, E., 2021. Depth–averaged and 3D Finite Volume numerical models for viscous fluids, with application to the simulation of lava flows. PhD thesis. University of Genova. https://doi.org/10.15167/biagioli-elisa_phd2021-10-27.

Bilotta, G., Cappello, A., Hérault, A. Vicari, Russo, G., Del Negro, C., 2012. Sensitivity analysis of the MAGFLOW cellular automaton model for lava flow simulation. Environ. Model Softw. 35, 122–131. https://doi.org/10.1016/j.envsoft.2012.02.015.

Bilotta, G., Cappello, A., Hérault, A., Del Negro, C., 2019. Influence of topographic data uncertainties and model resolution on the numerical simulation of lava flows. Environ. Model Softw. 112, 1–15. https://doi.org/10.1016/j.envsoft.2018.11.001.

Bilotta, G., Zago, V., Centorrino, V., Dalrymple, R.A., Hérault, A., Del Negro, C., Saikali, E., 2022. A numerically robust, parallel-friendly variant of BiCGSTAB for the semi-implicit integration of the viscous term in Smoothed Particle Hydrodynamics. J. Comput. Phys. 466 https://doi.org/10.1016/j.jcp.2022.111413.

Bonne, K., Kervyn, M., Cascone, L., Njome, S., Van Ranst, E., Shu, E., Ayonghe, S., Jacobs, P., Ernst, G., 2008. A new approach to assess long–term lava flow hazard and risk using GIS and low–cost remote sensing: the case of Mount Cameroon, West Africa. Int. J. Remote Sens. 29, 6539–6564. https://doi.org/10.1080/01431160802167873.

Boussinesq, J., 1877. Essai sur la théorie des eaux courantes. Impr. Nationale.

Cappello, A., Ganci, G., Calvari, S., Pérez, N.M., Hernández, P.A., Silva, S.V., Del Negro Cabral, J.C., 2016. Lava flow hazard modeling during the 2014–2015 Fogo eruption, Cape Verde. J. Geophys. Res. Solid Earth 121, 2290–2303. https://doi.org/10.1002/2015JB012666.

Chevrel, M.O., Favalli, M., Villeneuve, N., Harris, A.J.L., Fornaciai, A., Richter, N., Derrien, A., Boissier, P., Di Muro, A., Peltier, A., 2020. Lava flow hazard map of Piton de la Fournaise volcano. Nat. Hazar. Earth Syst. Sci. 21, 2355–2377. https://doi.org/10.5194/nhess-21-2355-2021.

Connor, L.J., Connor, C.B., Meliksetian, K., Savov, I., 2012. Probabilistic approach to modeling lava flow inundation: a lava flow hazard assessment for a nuclear facility in Armenia. J. Appl. Volcanol. 1 (3), 1–19. https://doi.org/10.1186/2191-5040-1-3.
Conroy, C.J., Lev, E., 2021. A discontinuous Galerkin finite–element model for fast channelized lava flows v1.0. Geosci. Model Dev. 14, 3553–3575. https://doi.org/10.5194/gmd-14-3553-2021.
Cordonnier, B., Lev, E., Garel, F., 2015. Benchmarking lava–flow models. Geol. Soc. Lond. Spec. Publ. 426 (71), 425–445. https://doi.org/10.1144/SP426.7.
Costa, A., Macedonio, G., May 2002. Nonlinear phenomena in fluids with temperature–dependent viscosity: an hysteresis model for magma flow in conduits. Geophys. Res. Lett. 29 (10), 401–404. https://doi.org/10.1029/2001GL014493.
Costa, A., Macedonio, G., 2003. Viscous heating in fluids with temperature–dependent viscosity: implications for magma flows. Nonlinear Process. Geophys. 10 (6), 545–555. https://doi.org/10.5194/npg-10-545-2003.
Costa, A., Macedonio, G., 2005. Numerical simulation of lava flows based on depth–averaged equations. Geophys. Res. Lett. 32 (5), L05304. https://doi.org/10.1029/2004gl021817.
Coulibaly, G., Leye, B., Tazen, F., Mounirou, L.A., Karambiri, H., 2020. Urban Flood Modeling Using 2D Shallow-Water Equations in Ouagadougou, Burkina Faso. In: Urban Flood Modeling Using 2D Shallow-Water Equations in Ouagadougou, Burkina Faso, 12(8). https://doi.org/10.3390/w12082120.
Courtney, R.C., White, R.S., 1986. Anomalous heat flow and geoid across the Cape Verde rise: evidence for dynamic support from a thermal plume in the mantle. Geophys. J. R. Astron. Soc. 87, 815–867.
Crisci, G.M., Di Gregorio, S., Pindaro, O., Ranieri, G.A., 1986. Lava flow simulation by a discrete cellular model: first implementation. Int. J. Model. Simul. 6, 137–140.
Crisci, G.M., Gregorio, S.D., Nicoletta, F.P., Rongo, R., Spataro, W., 1998. Cellular automata approaches for simulating rheology of complex geological phenomena. Cellul. Automata: Res. Towards Indus. 106–116. https://doi.org/10.1007/978-1-4471-1281-5_10.
G. M. Crisci, G. Iovine, S. Di Gregorio, and V. Lupiano. Lava–flow hazard on the SE flank of Mt. Etna (Southern Italy). J. Volcanol. Geotherm. Res., 177(4):778–796, nov 2008. doi: https://doi.org/10.1016/j.jvolgeores.2008.01.041.
Damiani, M.L., Groppelli, G., Norini, G., Bertino, E., Gigliuto, A., Nucita, S., 2006. A lava flow simulation model for the development of volcanic hazard maps for Mount Etna (Italy). Comput. Geosci. 32, 512–526. https://doi.org/10.1016/j.cageo.2005.08.011.
Darkwa, J., Suba, G., Kokkogiannakis, G., 2013. An investigation into the thermophysical properties and energy dynamics of an intensive green roof. J. Heat Mass Transf. 7, 65–84.
Davies, A.G., 2007. Volcanism on Io. Cambridge University Press.
Day, S.J., Heleno da Silva, S.I.N., Fonseca, J.F.B.D., 1999. A past giant lateral collapse and present–day flank instability of Fogo, Cape Verde Islands. J. Volcanol. Geotherm. Res. 94, 191–218. https://doi.org/10.1016/S0377-0273(99)00103-1.
de' Michieli Vitturi, M., Tarquini, S., 2021. MrLavaLoba: A new probabilistic model for the simulation of lava flows as a settling process. In: EGU General Assembly Conference Abstracts, 21, pp. 323–334. https://doi.org/10.1016/j.jvolgeores.2017.11.016.
de' Michieli Vitturi, M., Esposti Ongaro, T., Lari, G., Aravena, A., 2019. IMEX_SfloW2D 1.0. A depth–averaged numerical flow model for pyroclastic avalanches. Geosci. Model Dev. Discuss. https://doi.org/10.5194/gmd-2018-224.
de' Michieli Vitturi, M., Ongaro, T. Esposti, Engwell, S., 2023. IMEX_SfloW2D v2: a depth–averaged numerical flow model for volcanic gas–particle flows over complex topographies and water. Geosci. Model Dev. https://doi.org/10.5194/gmd-2023-80.
Deb Roy, G., Fazlul Karim, Md., Ismail, A.I.M., 2007. A nonlinear polar coordinate shallow water model for tsunami computation along North Sumatra and Penang island. Cont. Shelf Res. 27 (2), 245–257. https://doi.org/10.1016/j.csr.2006.10.004.
Del Negro, C., Fortuna, L., Herault, A., Vicari, A., Oct 2008. Simulations of the 2004 lava flow at Etna volcano using the MAGFLOW cellular automata model. Bull. Volcanol. 70 (7), 805–812. https://doi.org/10.1007/s00445-007-0168-8.
Dietterich, H.R., Lev, E., Chen, J., Richardson, J.A., Cashman, K.V., 2017. Benchmarking computational fluid dynamics models of lava flow simulation for hazard assessment, forecasting, and risk management. J. Appl. Volcanol. 6 (9), 1–14. https://doi.org/10.1186/s13617-017-0061-x.
Dionis, S.M., Perez, N.M., Hernández, P.A., Melián, G., Rodríguez, F., Padrón, E., Sumino, H., Barrrancos, J., Padilla, G.D., Fernandes, P., Bandomo, Z., Silva, S.V., Pereira, J.M., Semedo, H., Cabral, J., 2015. Diffuse CO2 degassing and volcanic activity at Cape Verde islands, West Africa. Earth Planets Space 67, 1–15. https://doi.org/10.1186/s40623-015-0219-x.
Dragoni, M., Borsari, I., Tallarico, A., 2005. A model for the shape of lava flow fronts. J. Geophys. Res. Solid Earth 110, B09203. https://doi.org/10.1029/2004JB003523.
Elong, A.J., Zhou, L., Karney, B., Fang, H., Cao, Y., Assam, S.L.Z., 2022. Flood Prediction with Two-Dimensional Shallow Water Equations: A Case Study of Tongo-Bassa Watershed in Cameroon. Appl. Sci. 12 (22) https://doi.org/10.3390/app122211622.
Fagents, S.A., Gregg, T.K.P., Lopes, R.M.C. (Eds.), 2012. Modeling Volcanic Processes. The Physics and Mathematics of Volcanism. Cambridge University Press.
Farmer, M.T., Sienicki, J.J., Spencer, B.W., 1990. The meltspread–1 computer code for the analysis of transient spreading in containments. Trans. Am. Nucl. Soc. 62, 644–646.
Favalli, M., Pareschi, M., Neri, A., Isola, I., 2005. Forecasting lava flow paths by a stochastic approach. Geophys. Res. Lett. 35, L03305. https://doi.org/10.1029/2004GL021718.
Felpeto, A., Marti, J., Ortiz, R., 2007. Automatic GIS–based system for volcanic hazard assessment. J. Volcanol. Geotherm. Res. 166, 106–116. https://doi.org/10.1016/j.jvolgeores.2007.07.008.
Fernández-Nieto, E.D., Garres-Díaz, J., Mangeney, A., Narbona-Reina, G., 2016. A multilayer shallow model for dry granular flows with the $\mu(i)$-rheology: application to granular collapse on erodible beds. J. Fluid Mech. 798, 643–681. https://doi.org/10.1017/jfm.2016.333.
Fernández-Nieto, E.D., Garres-Díaz, J., Mangeney, A., Narbona-Reina, G., 2018. 2d granular flows with the $\mu(i)$ rheology and side walls friction: A well-balanced multilayer discretization. J. Comput. Phys. 356, 192–219. https://doi.org/10.1016/j.jcp.2017.11.038.
Flynn, I.T.W., Chevrel, M.O., Crown, D.A., Ramsey, M.S., 2023. The effects of digital elevation model resolution on the PyFLOWGO thermorheological lava flow model. Environ. Model. Softw. 167 https://doi.org/10.1016/j.envsoft.2023.105768.
Fujita, E., Nagai, M., 2022. LavaSIM: its physical basis and applicability. Geol. Soc. 426, 375–386. https://doi.org/10.1144/SP426.14.
Ganci, G., Vicari, A., Cappello, A., Del Negro, C.., 2012. An emergent strategy for volcano hazard assessment: from thermal satellite monitoring to lava flow modeling. Remote Sens. Environ. 119, 197–207. https://doi.org/10.1016/j.rse.2011.12.021.
Garel, F., Kaminski, E., Tait, S., Limare, A., 2012. An experimental study of the surface thermal signature of hot subaerial isoviscous gravity currents: Implications for thermal monitoring of lava flows and domes. J. Geophys. Res. Solid Earth 117, B02205. https://doi.org/10.1029/2011JB008698.
Griffiths, R.W., 2000. The Dynamics of Lava Flows. Annu. Rev. Fluid Mech. 32, 477–518. https://doi.org/10.1146/annurev.fluid.32.1.477.
Gueugneau, V., Charbonnier, S., Esposti Ongaro, T., de' Michieli Vitturi, M., Peruzzetto, M., Mangeney, A., Bouchut, F., Patra, A., Kelfoun, K., 2021. Synthetic benchmarking of concentrated pyroclastic current models. Bull. Volcanol. 85, 1–32. https://doi.org/10.1007/s00445-021-01491-y.
Hager, W.H., Castro-Orgaz, O., Hutter, K., 2019. Correspondence between de Saint-Venant and Boussinesq. 1: Birth of the Shallow–Water Equations. Compt. Rend. Mecanique 347, 632–662. https://doi.org/10.1016/j.crme.2019.08.004.
Harris, A.J.L., Rowland, S., 2001. Flowgo: a kinematic thermo–rheological model for lava flowing in a channel. Bull. Volcanol. 63, 20–44. https://doi.org/10.1007/s004450000120.
Harris, A.J.L., Rowland, S.K., 2009. Effusion rate controls on lava flow length and the role of heat loss: a review. In: Studies in Volcanology: The Legacy of George Walker, 2. Special Publications of IAVCEI, pp. 33–51. https://doi.org/10.1144/IAVCEI002.3.
Harris, A.J.L., Favalli, M., Wright, R., Garbeil, H., 2011. Hazard assessment at Mount Etna using a hybrid lava flow inundation model and satellite–based land classification. Nat. Hazards 58, 1001–1027. https://doi.org/10.1007/s11069-010-9709-0.
Harris, A.J.L., Rhéty, Maéva, Gurioli, Lucia, Villeneuve, Nicolas, Paris, Raphaël, 2015. Simulating the thermo–rheological evolution of channel–contained lava: FLOWGO and its implementation in EXCEL. Geol. Soc. Lond., Spec. Publ. 426 (1), 313–336. https://doi.org/10.1144/SP426.9. ISSN 0305-8719.
Harris, A.J.L., De Groeve, T., Garel, F., Carn, S.A., 2016. Detecting, modelling and responding to effusive eruptions. Geol. Soc. Lond. Spec. Publ. 426, 1001–1027. https://doi.org/10.1144/SP426. 29.
Herault, A., Vicari, A., Ciraudo, A., Del Negro, C., May 2009. Forecasting lava flow hazards during the 2006 Etna eruption: using the MAGFLOW cellular automata model. Comput. Geosci. 35 (5), 1050–1060. https://doi.org/10.1016/j.cageo.2007.10.008.
Hergarten, S., Robl, J., 2015. Modelling rapid mass movements using the shallow water equations in Cartesian coordinates. Nat. Hazards Earth Syst. Sci. 15, 671–685. https://doi.org/10.5194/nhess-15-671-2015.
Hogg, A.J., Pritchard, D., 2004. The effects of hydraulic resistance on dam–break and other shallow inertial flows. J. Fluid Mech. 501, 179–212. https://doi.org/10.1017/S0022112003007468.
Huppert, H.E., 1982. The propagation of two–dimensional and axisymmetric viscous gravity currents over a rigid horizontal surface. J. Fluid Mech. 121, 43–58.
Hyman, D.M.R., Dietterich, H.R., Patrick, M.R., 2022. Toward next–generation lava flow forecasting: development of a fast, Physics–Based Lava propagation model. JGR: Solid Earth 127. https://doi.org/10.1029/2022JB024998 e2022JB024998.
Kauahikaua, J., Cashman, K., Mattox, T., Heliker, C., Hon, K., Mangan, K., Thornber, C., 1998. Observation on basaltic lava streams in tubes from Kilauea Volcano, island of Hawai'i. J. Geophys. Res. 103, 27303–27323. https://doi.org/10.1029/97JB03576.
Kelfoun, K., Vargas, S.V., 2016. VolcFlow capabilities and potential development for the simulation of lava flows. Geol. Soc. Lond. Spec. Publ. 426 (1), 337–343. https://doi.org/10.1144/SP426.8.
Kilburn, C.R.J., 1999. Lava Flows and Flow Fields. In: Encyclopedia of Volcanoes, pp. 291–305.
Kolzenburg, S., Giordano, D., Di Muro, A., Dingwell, D.B., 2018. Equilibrium viscosity and disequilibrium rheology of a high magnesium basalt from piton de la fournaise volcano. Ann. Geophys. 61 https://doi.org/10.4401/ag-7839.
Kosky, P., Balmer, R., Keat, W., Wise, G., 2013. Exploring Engineering, 3 edition. Academic Press (ISBN 9780124158917.).
Kubanek, J., Richardson, J.A., Charbonnier, S.J., Connor, L.J., 2015. Lava flow mapping and volume calculations for the 2012–2013 Tolbachik, Kamchatka, fissure eruption using bistatic TanDEM–X InSAR. Bull. Volcanol. 77 (106), 1–13. https://doi.org/10.1007/s00445-015-0989-9.
Kurganov, A., Petrova, G., 2007. A second–order well–balanced positivity preserving central upwind scheme for the Saint–Venant system. Commun. Math. Sci. 5 (1), 133–160.
LeVeque, R.J., 2002. Finite volume methods for hyperbolic problems. Cambridge university press.
Lister, J.R., 1992. Viscous flows down on inclined plane from point and line sources. J. Fluid Mech. 242, 631–653. https://doi.org/10.1017/S0022112092002520.

Michel, B.D., Piar, B., Babik, J.C., Latche, F., Guillard, G., De Pascale, C., 2000. Synthesis of the validation of croco v1 spreading code. Proceed. OECD Workshop Ex–Vessel Debris Coolabil. 6475, 235–245.

Modest, M.F., 1993. Radiative Heat Transfer. McGraw–Hill, New York.

Nakamura, Y., Aoki, K., 1980. The 1977 eruption of Nyiragongo volcano, eastern Africa, and chemical composition of the ejecta. Bull. Volc. Soc. Jpn 25 (1), 17–32. https://doi.org/10.18940/kazanc.25.1_17.

Pareschi, L., Russo, G., 2000. Implicit–Explicit Runge–Kutta schemes for stiff system of differential equations. In: Recent Trends in Numerical Analysis. Nova Science, pp. 269–288.

Patrick, M.R., Dehn, J., Dean, K., 2004. Numerical modeling of lava flow cooling applied to the 1997 Okmok eruption: Approach and analysis. J. Geophys. Res. 109, B03202. https://doi.org/10.1029/2003JB002537.

Pedersen, G.B.M., Höskuldsson, A., Dürig, T., Thordarson, T., Jonsdottir, I., Riishuus, M. S., Óskarsson, B.V., Dumont, S., Magnusson, E., Gudmundsson, M.T., Sigmundsson, F., Drouin, V.J.P.B., Gallagher, C., Askew, R., Gudnason, J., Moreland, W.M., Nikkola, P., Reynolds, H.I., Schmith, J., Sigmundsson, F., 2017. Lava field evolution and emplacement dynamics of the 2014-2015 basaltic fissure eruption at holuhraun, Iceland. J. Volcanol. Geotherm. Res. 340, 155–169.

Pinkerton, H., Wilson, L., 1994. Factors controlling the lengths of channel-fed lava flows. Bull. Volcanol. 56, 108–120. https://doi.org/10.1007/BF00304106.

Rhéty, M., Harris, A.J.L., Villeneuve, N., Gurioli, L., Médard, E., Chevrel, M.O., Bachèlery, P., 2017. A comparison of cooling–limited and volume–limited flow systems: examples from channels in the Piton de la Fournaise April 2007 lava–flow field. Geochem. Geophys. Geosyst. 18 (9), 3270–3291. https://doi.org/10.1002/2017GC006839.

Richter, N., Favalli, M., de Zeeuw-van Dalfsen, E., Fornaciai, A., da Silva Fernandes, R. M., Pérez, N.M., Levy, J., Silva, S.V., Walter, T.R., 2016. Lava flow hazard at Fogo Volcano, Cabo Verde, before and after the 2014–2015 eruption. Nat. Hazards Earth Syst. Sci. 16, 1925–1951. https://doi.org/10.5194/nhess-16-1925-2016.

Rizzoli, P., Martone, M., Gonzalez, C., Wecklich, C., Borla Tridon, D., Bräutigam, B., Bachmann, M., Schulze, D., Fritz, T., Huber, M., Wessel, B., Krieger, G., Zink, M., Moreira, A., 2017. Generation and performance assessment of the global TanDEM–X digital elevation model. ISPRS J. Photogramm. Remote Sens. 132, 119–139. https://doi.org/10.1016/j.isprsjprs.2017.08.008.

Russo, G., 2000. Central schemes for balance laws, hyperbolic problems: theory, numerics, applications. Int. Ser. Numer. Math. 141, 821–829. https://doi.org/10.1007/978-3-0348-8372-6_35.

Russo, G., 2005. Central schemes for conservation laws with application to shallow water equations. In: Romano, G., Rionero, S. (Eds.), Trends and Applications of Mathematics to Mechanics. The Organization, Springer, pp. 225–246. https://doi.org/10.1007/88-470-0354-7_18.

Tallarico, A., Dragoni, M., 2000. A three-dimensional bingham model for channeled lava flows. J. Geophys. Res. Solid Earth 105 (B11), 25969–25980.

Tang, H.S., Kalyon, D.M., 2004. Estimation of the parameters of Herschel–Bulkley fluid under wall slip using a combination of capillary and squeeze flow viscometers. Rheol. Acta 43, 80–88. https://doi.org/10.1007/s00397-003-0322-y.

Tarquini, S., Favalli, M., 2011. Mapping and downflow simulation of recent lava flow fields at Mount Etna. J. Volcanol. Geotherm. Res. 204, 27–39. https://doi.org/10.1016/j.jvolgeores.2011.05. 001.

Toro, E.F., 1990. The dry bed problem in shallow water flows. College Aeronaut. Report No. 9007.

Turcotte, D.L., Shubert, G., 1982. Geodynamics. Cambridge University Press.

Vicari, A., Alexis, H., Del Negro, C., Coltelli, M., Marsella, M., Proietti, C., 2007. Modeling of the 2001 lava flow at Etna volcano by a cellular automata approach. Environ. Model Softw. 22 (10), 1465–1471. https://doi.org/10.1016/j.envsoft.2006.10.005.

Wadge, G., Young, P.A.V., McKendrick, I.J., 1994. Mapping lava flow hazards using computer simulation. J. Geophys. Res. Solid Earth 99, 489–504. https://doi.org/10.1029/93JB01561.

Xia, X., Liang, Q., 2018. A new depth–averaged model for flow–like landslides over complex terrains with curvatures and steep slopes. Eng. Geol. 234, 174–191. https://doi.org/10.1016/j.enggeo.2018.01. 011.

Young, P., Wadge, G., Jan 1990. FLOWFRONT: simulation of a lava flow. Comput. Geosci. 16 (8), 1171–1191. https://doi.org/10.1016/0098-3004(90)90055-X.

Zago, V., Bilotta, G., Cappello, A., Dalrymple, R.A., Fortuna, L., Ganci, G., Herault, A., Del Negro, C., 2019. Preliminary validation of lava benchmark tests on the GPUSPH particle engine. Ann. Geophys. https://doi.org/10.4401/ag-7870.